AN INVERSE ACOUSTICAL PHASED ARRAY TECHNIQUE

FOR IMPACT DETECTION AND LOCATION

by

Tyler Steven Papulak

A thesis submitted to the faculty of
The University of Utah
in partial fulfillment of the requirements for the degree of

Master of Science

Department of Civil and Environmental Engineering

The University of Utah

May 2012

The University of Utah Graduate School

STATEMENT OF THESIS APPROVAL

The thesis of **Tyler Steven Papulak**

has been approved by the following supervisory committee members:

Paul Tikalsky	, Chair	**1/6/2012** Date Approved
Chris Pantelides	, Member	**1/6/2012** Date Approved
Daniel O. Adams	, Member	**1/6/2012** Date Approved
Chris Deemer	, Member	**1/6/2012** Date Approved

and by **Paul Tikalsky** , Chair of the Department of **Civil and Environmental Engineering**

and by Charles A. Wight, Dean of The Graduate School.

ABSTRACT

Due to the complex failure modes associated with composites, a structural health monitoring system capable of accurately locating the source of strength-reducing events is desirable in order to reduce inspection time and time out of service. Various active and passive inspection techniques exist but most require large footprints and extensive cabling to monitor full scale structures. This work derives various location techniques by coupling modal acoustic emissions with phased array techniques to detect and accurately locate the source of strength-reducing events such as impacts. Phased array techniques provide a method to more accurately track phase points for determining arrival times used to back-calculate the source, as well as providing a method that can incorporate anisotropic wave speeds. To increase accuracy by neglecting local to global material changes, the local velocity profile per component was found and built into the derived location algorithms. The location algorithms were then tested on two full scale composite structures based on strength and stiffness critical design considerations. It was found that with two arrays, each with dimensions of 1 inches in width and 8 inches in length and consisting of four sensors each, events could be accurately located over a 65 ft^2 region on the stiffness critical structure with an average error of 10 inches and over a 100 ft^2 region on the strength critical structure with an average error of 9 inches.

TABLE OF CONTENTS

LIST OF TABLES

Table Page

LIST OF FIGURES

Figure Page

SYMBOLS

C_l – Longitudinal Bulk wave velocity

C_t – Transverse Bulk wave velocity

d – Plate thickness

E – Young's modulus

f – Frequency

k_l- Longitudinal wave number

k_t- Transverse wave number

k_a- Anti-symmetric Lamb wave number

k_s- Symmetric Lamb wave number

t – Time

Δt- Change in time

v – Velocity

V – Particle displacement vector

υ - Poison's ratio

ω- Angular frequency

λ_l – Longitudinal wavelength

λ_t – Transverse wavelength

θ- Angle

ϕ- Phase shift

Φ and ψ – displacement potentials (Helmholtz theorem)

ABBREVIATIONS

AE – Acoustic emissions

AIMS – Automated impact monitoring system

BDD – Barely detectable damage

BVD – Barely visible damage

CRFP – Carbon fiber reinforced plastic

FE – Finite element

FTP – File transfer protocol

LAN – Local area network

MAE – Modal acoustic emissions

PCB – Printed circuit board

Q – Measure of a sensors frequency response

SHM – Structural health monitoring

STMR – Single transmitter multiple receiver

TOF – Time of flight

ACKNOWLEDGEMENTS

I would like to extend my thanks to ATK and the Air Force Research Lab (AFRL) for providing the equipment and funding necessary to perform this work. In particular, I am grateful to ATK for providing me with a job while I finished my degree and funding my efforts in school. To my boss, Don Gardiner, I would like to thank you for opening the door for me to the world of acoustic emissions and bringing me on as part of your team; it was a great honor. Your knowledge and insight in inspection knows no bounds. Joe Paustenbaugh, I owe you the world for helping me get my foot in the door, providing me with the opportunity to learn from such great people.

I would also like to thank Digital Wave Corporation for their time and effort during this study and in particular, Mike Gorman, Steve Ziola, and Michael Malak. Mike Gorman and Steve Ziola, you provided me with a vast amount of knowledge and help regarding modal acoustic emissions as well as many insightful articles to expand my knowledge. Mike Malak, thanks to your software development, you saved me countless hours determining phase points and arrival times.

I would also like to provide a special thanks to Chris Deemer who was my mentor and guide throughout this whole project without whom I would be lost. Thanks for all

your time and effort over all the years and answering my many annoying questions. Thanks for guiding me through this process.

Also, thanks for all you support Dr. Tikalsky. Without your help, I may have never made it to where I am. You helped me develop a very particular curriculum that wouldn't have been possible without your support. Also, I would like to thank the rest of my committee for their support. I know it was a long thesis and I am grateful for your support and hoped you learned as much as I have from writing this.

I would also like to thank my parents, Steve Papulak and Malinda Mitchell. Dad, without your financial support and drive over all the years, I may have never made it this far. Mom, thanks for helping me throughout all these years, your love will always be appreciated.

I would also like to acknowledge my friends, Cory Olsen and Dan Morgan, for their support over all the years. You provided me with an escape when I needed time to free my mind.

CHAPTER 1

INTRODUCTION

1.1 Rational

Composites are becoming widely used in aeronautic and aerospace applications. One of the prime issues in the implementation of polymer-based composites into aeronautic and aerospace applications are the complex failure mechanisms combined with composites capability to contain nonvisible performance-reducing damage. In particular, a prime concern for designers and end-users is impact-induced damage (1). Great efforts are taken to reduce risk from damage induced during fabrication including full nondestructive inspection and proof testing (2). These steps are usually taken at the manufacturing facility whereas damage can be induced during transport, installation, and in service. In addition, it is possible that out-of-design loading may cause no visual indications but still initiate performance-reducing damage in service (1).

Traditionally, this has been accounted for by designing for Barely Visible Damage (BVD) by increasing the factors of safety. To reduce weight and manufacturing costs, attempts are being made to design to Barely Detectable Damage (BDD) (3). Decreasing the critical damage size to BDD implies that steps must be taken to reduce the risk of

damage initiation induced after the component leaves the manufacturing facility to when it is put into service. Although designing to BDD decreases manufacturing costs, maintenance costs are increased to ensure the safety of the component. For these reasons, it is desirable to develop a system capable of monitoring the structural integrity of composite structures throughout their life cycle.

There are two primary means of reducing the risk of strength-reducing impact damage in full-scale composite components in service: 1) increase factors of safety during the design process enabling the component to be unaffected by damage induced by impact events, fatigue, and corrosion and 2) implement a system capable of monitoring the health of the material known as Structural Health Monitoring (SHM). Increasing the factors of safety, in essence overdesigning the component, increases material cost, component weight, and fabrication schedule. Therefore, it is desirable to develop a system capable of monitoring the structures performance capabilities during transport and service.

Two types of SHM systems are utilized to monitor structures/components: 1) passive and 2) active systems. Passive systems remain dormant "listening" for damage to occur in real time where active systems are used to physically search for damage (traditional NDT techniques such as ultrasound are an example of an active method). Active systems can be small and unobtrusive; however, inspection can be time-consuming and costly unless the source of damage is already known. Passive systems on the other hand can locate the source of damage but require integration of high

sensor densities to cover large structures which can also make them cost-prohibitive, complex, and require large footprints on the component.

Impact detection and locating has been using Acoustic Emissions (AE) since 1976 using triangulation techniques (4). This methodology for source locating requires the sensors to be spread at various locations across the surface of the component and is most accurate when the event is contained within the bounds of the sensor configuration. This implies that a large number of sensors are required to ensure coverage of full-scale components and that these sensors would need to be distributed about the part. The number of sensors and their disperse locations requires triangulation-based location techniques to have large footprints and large amounts of cabling to connect the sensors to the data acquisition system. Furthermore, triangulation-based algorithms do not take into account the anisotropic nature of the propagating wave in anisotropic material systems. Anisotropy can be included; however, the solution becomes complicated and can introduce more errors.

As a means of mitigating these issues, the objective of this work is to refine a low profile, low sensor density impact detection system that has a very small surface area footprint. This system will utilize a passive Modal Acoustic Emissions (MAE) system to detect and locate impacts on full-scale anisotropic composite components. The system will have the capability to detect strength reducing events that may occur due to out-of-design loading, impact, or crack propagation.

1.2 Objective

The objective of this effort has been to develop an integrated health monitoring system for composite structures to detect and locate strength-reducing events using modal acoustic emission technology. MAE is a method of measuring sound wave propagation in composite laminates. When energy is imparted (e.g., from impact) or released (e.g., part fracture) in a composite, two distinct waves are created, an extensional wave and a flexural wave (5). The extensional wave is characterized by high frequency, high velocity, and particle motion primarily in plane in the direction of wave propagation resulting in high attenuation. The flexural wave exhibits lower velocity, and lower attenuation due to particle motion principally orthogonal to the direction of propagation.

To increase accuracy, while decreasing the sensor/cabling requirements, the system that is being investigated in this study utilizes phased array technology coupled with MAE to develop a low profile, small surface area, low sensor density impact detection system. This document describes algorithms based on beam steering and focusing techniques used in ultrasonic phased array to more accurately locate strength-reducing events on composite structures. The theory uses passive MAE to detect events and from waveform analysis, determine arrival times that are used in the location algorithms to perform estimated impact location.

1.3 Approach

Using MAE, a system is to be designed to detect and locate strength-reducing events. First, various impacts are needed to characterize how the wave modes propagate throughout the component being tested. Once the wave characteristics have been identified, the next step is to configure an array of sensors on the component to optimize the ability of the sensors to detect impacts from all locations on the component. The dispersion curves then need to be determined for the frequencies characteristic to the component as well as their attenuation characteristics. Then using the concepts of triangulation and phased array, a technique used to locate impacts will be formulated and tested on two full-scale composite components provided by ATK Aerospace Corporation[1].

It is of note, however, that this system will not identify the extent of the damage as this is a complex problem suggested for future work. Instead, this system is designed to monitor the component throughout all stages of life. When an impact or other event takes place, the system will activate, locate the event, and inform the responsible engineer for further damage analysis. This technique will decrease inspection times by notifying the responsible engineer when possible damage occurs and directing them to the approximate area in which more sophisticated techniques of damage characterization can be performed.

---

[1] ATK Aerospace Systems Aerospace Structures Division, Freeport Center, Building C14, Clearfield, UT USA 84016; 801-775-1262

CHAPTER 2

LITERATURE REVIEW

The following literature review is intended to provide the reader with an overview of the various methods used for damage detection and location. First, the use of acoustic emissions for the detection of damage propagation is reviewed, followed by an overview of the various impact damage detection methods using both passive and active systems. The last section provides the reader with a basic understanding of how phased array ultrasonic's works. More on this topic will be discussed later as it is used to derive the location algorithms used in this work.

2.1 Acoustic Emissions

In 1991, Gorman suggested that plate waves can be used to better understand Acoustic Emission (AE) phenomena, as seen in Figure 1 (6). In the limit that the wavelength of a linearly elastic displacement is much larger than the plate's thickness, a simple set of equations derived from classical plate theory is used to understand wave motion. This is known as the "thin plate" approximation and the resulting waves are called plate waves. Plate waves consist of two modes of propagation (extensional and flexural modes). Both modes have in-plane and out-of-plane components due to the

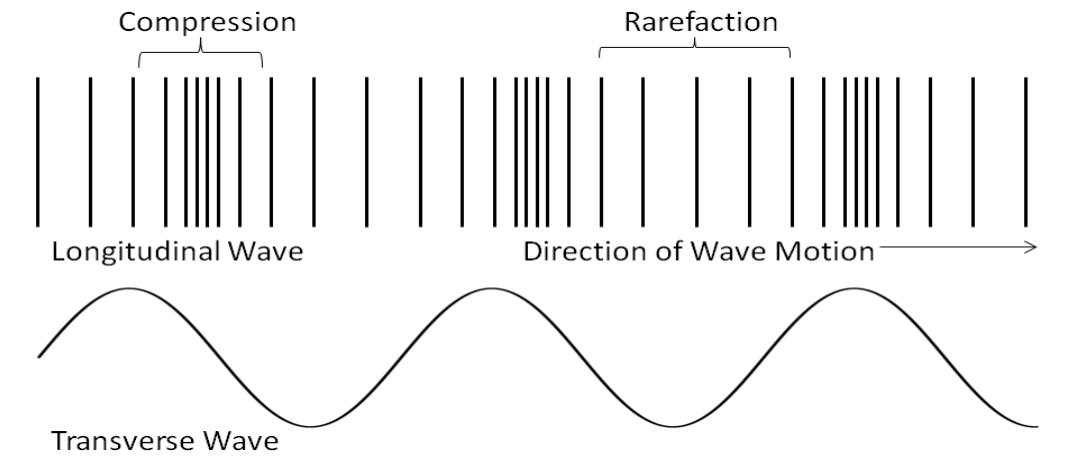

(A)

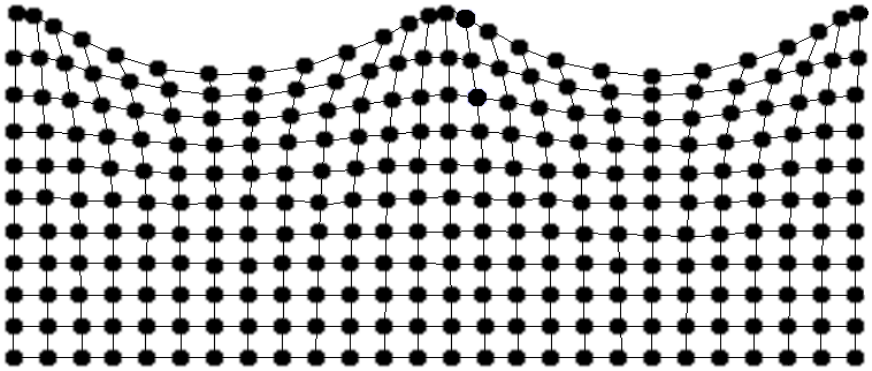

(B)

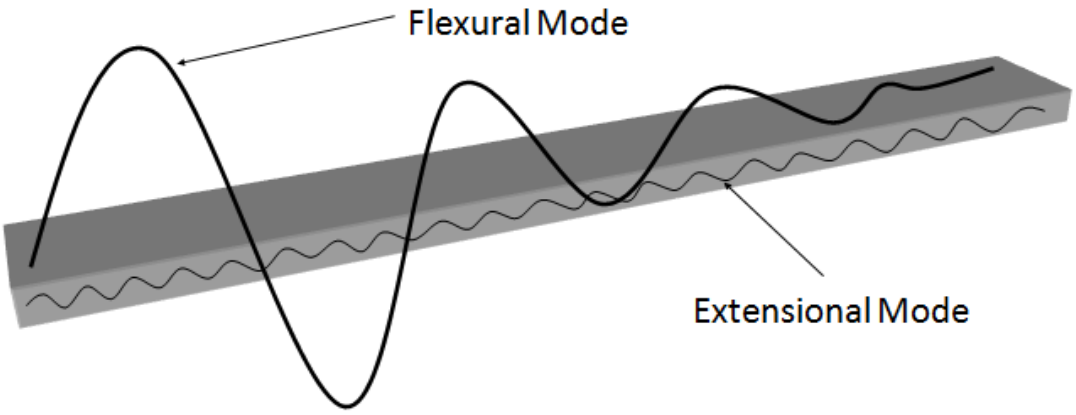

(C)

Figure 1. Various types of elastic waves that can occur in solids: A) bulk waves, B) Rayleigh or surface wave, and C) guided plate waves.

Poisson effect. The extensional (symmetrical) mode has the largest displacement component occurring in the plane of the plate and travels at a much higher velocity and typically consists of higher frequency components. The extensional wave is not as dispersive in nature and is therefore better for accurate source location but attenuates much faster. The flexural (antisymmetrical) mode is what is typically measured using AE due to its much larger out-of-plane component. The flexural mode typically consists of lower frequencies and velocities due to its out-of-plane components and will thus travel much larger distances. This makes the flexural wave better for location determination in large scale structures; however, it is much more difficult due to its dispersive nature, unlike the extensional mode. Gorman also shows that acoustic emissions produced by matrix cracks in composites do in fact result in plate waves and as such, plate waves can be used to better increase our understanding of damage formation and location techniques of damage formed in composites.

Later in 1991, Gorman, Prosser, and William investigated the use of MAE for source orientation of acoustic emission sources (7). Using a Hsu-Neilson source (lead brake), AE signals were generated in an aluminum plate at multiple angles with respect to the plane of the plate. The various orientations were formed by cutting slots into the plate at the various angles. They found that the amplitudes of the two modes were different when the lead brake was applied at the edge of the plate versus the surface. The authors found there was a relationship between the source orientation angle to the amplitudes of both the extensional and flexural modes. For smaller angles from the plane of the plate, the largest component from the source was the in-plane component

of the extensional mode. For larger angles, the flexural wave amplitude was more dominant. The authors found two major results. First, the flexural wave amplitude was much more dominate at 60 degrees than any other source orientation for reasons not yet understood. Second, even at large source angles where it should be the largest, the in-plane component of the flexural mode is not detected. The extensional wave out-of-plane components can be detected for all observed source angles. The researchers also discovered that use of a broad band transducer detects the different modes much better then narrow band resonate AE transducers due to the ringing in the transducer leading to indistinguishable modes. In conclusion, the authors stated that measuring the amplitudes of the plate modes should allow determination of the angle and energy of the impact which results in better estimation of damage. By considering the effects of plate wave propagation, more accurate source location algorithms can be obtained in composites.

Rogers described a technique used to solve the inverse problem, i.e., from experimental measurements of frequency and phase velocity determining Young's modulus and Poisson's ratio (8). The technique is demonstrated on aluminum, steel, and glass plates ranging in thickness of 0.24 inches to 0.03 inches. Lamb waves are used due to their lower attenuation and long travel distances and the fact that a broad range of frequencies can be used. Due to the nature in which Lamb waves travel, they can also be used to measure the out-of-plane properties as well. For a particular frequency, the phase velocity is determined as a function of angle by using a pair of contact transducers and measuring the phase shift of the harmonic waves over a measured

distance. Then, using the phase velocity versus frequency measurements, the inverse problem is solved by using a nonlinear least squares algorithm. Rogers found that the nonlinear behavior of the dispersion equations lead to slightly inaccurate results and therefore, by properly selecting fewer frequency-phase velocity points, more accurate estimates of the material constants could be found. The uncertainty in the estimation of the Young's modulus was found to be less than 1% and the uncertainty in Poisson's ratio was less than 2%. Rogers states that the advantages of this method over others are great for composites since material properties vary with frequency, the thin nature of composite structures, and the need to use wavelengths greater than the plate's thickness.

Andreikiv, Skal's'kyi, and Serhienko explored previous results from fracture mechanics using AE to monitor the development of damage and present methods used to establish criteria for estimation of fracture and volume damage of composite materials (9). The tests were performed on composite plates of carbon fiber with various stacking sequences of 16 layers and an epoxy resin. The plates were 3.94 x 0.79 x 0.08 inches in size and tested by a three point bending test cycle. AE was found to be highly sensitive and efficient in the diagnosis of structures independent of form and size. Under loading, the AE activity was found to vary under the various types of stacking sequences. However, some criteria were established to estimate fracture and volume of damage. The authors found that in all composite materials, the initial stages of fracture was low, signified by low amplitude AE signals associated with exfoliation along the fiber-matrix surface. The next stage was related to higher amplitude signals

associated with matrix cracking. The authors found that typically, there exists a threshold deformation at the beginning of these two stages. They found that the time at which the damage reaches a certain level depends on the load history of the composite. By monitoring the sum of the amplitudes, the formation and growth of internal damage can be seen. The volume of damage highly affects the attenuation of AE signals. Therefore, the criteria for estimation of volume damage in composites are as follows: a) monitoring for abrupt changes in amplitudes, b) sum of amplitudes, and c) losses due to attenuation during the load cycle. Using the basic criteria, the service life of the material can be monitored. The authors show that AE is sensitive to the dynamics of damage formation in composites both in the micro and macro fracture processes.

2.2 Impact Damage Detection Methods

Guo and Cawley discuss how interactions of the symmetrical Lamb mode with delaminations can be used to detect defects in composite laminates (10). Tests were performed on an eight layer cross-ply laminate of stacking sequence $[(0,90)_2]_S$ (see Appendix A for more on ply orientation code) where each layer was 0.0049 inches thick. The symmetrical Lamb mode can propagate over large distances as compared to the traditionally used ultrasonic C-scan. C-scans are time-consuming for inspection since the area being inspected is limited by the diameter of the transducer used. Lamb modes propagate in the plane of the plate and therefore, large regions can be scanned per transducer position. However, due to the nature of Lamb mode propagation, vibration patterns are mode and frequency dependent. Here, the authors investigate

the reflectivity of the Lamb modes on delaminations at different thicknesses. They found that Lamb mode interactions depend on the delamination position through the laminate thickness. Some positions did not generate a reflection; however, they still can be predicted by calculating the shear stress distribution across the thickness of the laminate. The authors note that delaminations at different thicknesses cannot be found using a single Lamb mode and therefore, it is necessary to detect delaminations in the thickness using multiple tests and modes. This can be bypassed, however, for many applications such as impact damage. Impact damage typically spreads over many layers and a single mode can be used to detect the damaged area. The advantages of this method over traditional C-scans are that larger area can be covered per pass and that the area under interrogation at any instant is not limited to the region covered only by the transducer.

Kessler, Spearing, and Soutis explore the application of Lamb wave methods for damage detection and the path for optimizing the system (11). They explored the effects that various parameters have on the ability to detect damage and how the excitation pulse parameters such as shape, amplitude, frequency, and the cycles present within each pulse affect the ability to locate damage. It was found that more accurate wave speed calculations are achieved by higher energy driving frequencies. The geometry and material properties were also investigated in this study. It was found that the antisymmetrical mode is fairly invariant to the composites layup and can be approximated using the bulk laminate properties. The Lamb wave's group velocity was found to be sensitive to areas of reduced stiffness and will slow down. Using specimens

with various forms of damage such as delamination, matrix cracks, and through thickness holes, the ability of Lamb waves to detect damage was shown. Kessler et al. showed that their method is more sensitive to damage locally then the previously used frequency response method (11).

Diamanti, Hodgkinson, and Soutis explore the ability to detect low velocity impacts by exciting the antisymmetrical Lamb mode to successfully detect and locate damage sites by transmitting and receiving the antisymmetric Lamb mode (12). A Finite Element (FE) model was used to replicate the experiment and determine the array spacing for the transmitter/receiver sensor pair. Once the setup was verified, the authors used thin piezoelectric elements, operating mainly in the longitudinal mode, to generate and monitor the antisymmetrical Lamb mode at low frequencies. Low frequencies were used because their low attenuation allowed the sensors to be used without amplifiers reducing cost. In both the FE model and the experimental results, damage detection and location were possible using the amplitude of the reflected signal and Time of Flight (TOF). It was found that damage in the direction perpendicular to the array was detectable and that location of the damage was accurate; however, the damage extent in the direction parallel to the array was not accurate due to the wave propagation across the width of the plate producing noise between the excitation and reflection from the back edge of the plate.

Using work done on previous studies of impact damage, Toyama and Takatsubo designed a new method for detection of delaminations and to evaluate crack size and location (13). The method utilized Lamb wave velocity and attenuation, in two scans.

Experiments were performed on T800H/3631 (Toray carbon fiber/Toray epoxy resin) carbon fiber reinforced plastic (CFRP) cross ply laminates with stacking sequences of $[0/90_3]_s$ and $[0/90]_{2s}$. Delaminations are created by low velocity impacts. The first scan transmits the symmetrical mode along the 0^o direction before and after the impacts and measures the distribution of the arrival times. Using this data set, the authors were able to detect delaminations and evaluate the size of the damaged area. The second scan allows location to be determined of the delamination edge by measuring the transition of the maximum amplitude of the earliest wave packet. Using basic models of Lamb wave propagation, the delamination length can be determined. The prevalent type of damage found in composite structures is internal damage from low velocity impacts and as such, the authors deduced using low velocity impacts while delamination was used since it caused significant loss of compressive strength and stiffness. The symmetrical mode was used since in the frequency thickness product range below 1 MHz mm, the symmetrical mode is almost nondispersive while the antisymmetrical mode is highly dispersive. The symmetrical mode is also highly dependent on the in-plane stiffness and is highly sensitive to detecting stiffness changes. The authors found that in both cross-ply and quasi-isotropic laminates, the elliptical delamination initiates on the interface opposite the impact and propagates in the fiber direction. The reason for placing the sensors in the 0^o direction is that the in-plane stiffness of the 0^o layer is the highest and the wave velocity increases in the delaminated region, increasing the sensitivity of the symmetrical mode velocity and amplitude. Using conventional C-scans, the results were

validated confirming the potential of this method as a quick inspection technique for impact-induced delamination in anisotropic structures.

Diamanti, Soutis, and Hodgkinson, in 2005, used low frequency Lamb waves to detect and locate critical damage size in CFRP beams and sandwich structures (14). Experiments were carried out on: four CFRP beams of lay-ups $[0]_8$, $[90]_{16}$, $[45/-45]_{4s}$, and $[45/0/-45/90]_{2s}$ T700UD/SE84HT (Toray carbon fiber/SP Systems epoxy resin) carbon fiber epoxy resin system prepreg tape and a quasi-isotropic sandwich beam with skin layup $[[45/-45/0/90]_{2s}$ and three different 0.39 inch thick cores made up of aluminum, and two types of Rohacell foam (R51 and R71). The dimensions of the beams were approximately 0.79 inch wide by 17.72 to 23.62 inches in length. Using small piezoceramic patches, the antisymmetric Lamb mode antisymmetrical is transmitted at frequencies below 50 kHz and received to detect and locate damage. The beams were pre-impacted and due to the different lay-ups, many different damage types were studied. The authors show that in both the monolithic and sandwich beams, critical damage can be successfully detected and located. The resolution is poor and this method cannot separately identify closely spaced damage areas. This method, however, can be used as a first stage detection of global damage detection and location then used in combination with a more sensitive technique to accurately characterize the damage when necessary.

Diamanti et al. (2007) presented ongoing work to develop a system that can be permanently attached to a composite structure for monitoring damage by use of low frequency Lamb waves and their interactions with defects (15). Tests were carried out

on a sixteen ply quasi-isotropic carbon fibre reinforced plastic laminate $[+45/0/-45/90]_{2S}$. Using a linear array of transmitters, the fundamental antisymmetric Lamb mode (A_0) was generated at 20 kHz to inspect large areas with a limited number of transducers. The array of transducers was used to generate a uniform wave front as well as to receive the reflected wave and therefore detect and locate damage using the amplitude of the reflected signals and time of flight information, respectively. The lower frequency reduces the resolution of inspection; however, it attenuates less and therefore does not need amplifiers which reduce cost and weight of the equipment. Low velocity impacts of critical size (0.79 – 0.98 inches in diameter) were identified using this procedure. Using the linear array location of the damage perpendicular to the array was successfully determined (laminate length) but the width was not determined. To determine the width, a second array should be placed perpendicular to the first array.

In 2009, Vishnuvardhan, Muralidharan, Krishnamurthy, and Balasubramaniam demonstrated two methods to (a) measure elastic moduli and (b) image edges and defects in anisotropic composites (16). Both utilized flexible printed circuit board (PCB)-patches for single transmitter and multiple receiver (STMR) arrays. Experiments were carried out on a 0.12 inch graphite/epoxy plate. Due to degradation of elastic moduli (time dependent and damage dependent) the authors found it necessary to measure current moduli for use in the phased addition algorithm for imaging defects. For assessment of elastic moduli, a single quadrant double ring STMR array was developed to gather data for a GA-based inversion method using the antisymmetrical mode

velocities measured in various directions. It was found that elastic moduli was more sensitive to the use of Lamb wave velocities and had many advantages over the use of bulk wave velocity data such as: no need to immerse the sample, increased sensitivity, and can be used as an in-situ ultrasonic Lamb wave method. Using the newly assessed elastic moduli, a full ring STMR array was used with a phased addition reconstruction algorithm to successfully image damage and edges present in anisotropic plate-like structures. The algorithm took into account the anisotropic nature of the material and accurately imaged defects in the near and far field regions of the plate. The authors generalized the algorithm for image reconstruction using an array of any configuration.

2.3 Phased Array

In 1993, Ramm and Smith discuss the principals and techniques used in phased array ultrasound scanners used in the practice of modern medicine (17). The main topics discussed in this work were the geometric optics employed in beam steering and focusing of linear arrays in the transmit and receive mode. A linear array is a transducer made of a number of tightly packed piezoelectric elements. The elements typically are cut from a single piezoelectric plate where the operating frequency is determined by the thickness of the plate. Images are produced by utilizing all the elements in the array by rapidly steering the acoustic beam through the material by electronic means. The array aperture can be electronically focused to receive at several points improving scan resolutions as well as for parallel processing to increase data rates. Beam steering allows the user to control the direction of propagation by altering the timing sequence

of the excitation pulses. By linearly exciting the pulses in each element within the array, the individual acoustic wave fronts will constructively add up to create a maximum intensity in the direction desired. Beam focusing employs the same concept; however, the timing relationship combines the linear pulse excitation with a spherical one which results in a beam that can be focused at a given range and propagate at a specific azimuthal angle.

Using a model developed to compute acoustic pressure distribution of waves radiated from ultrasonic linear phased array, beam directivity and steering was studied by Wooh and Yijun for different transducer parameters (18). The various parameters included interelement spacing, element width, transducer frequency, and the number of elements. The authors found that interelement spacing was important for determining transducer performance as well as the number of elements. The steering ability is the most important factor in determination of transducer characteristics. Steering ability is affected by center frequency, element size or width, and as mentioned above, the number of elements as well as interelement spacing. By increasing the number of elements, beam directivity is enhanced. The authors found that for full 180^0 steering, the interelement spacing selected should be smaller than half of the wavelength. If full 180^0 steering is not required, however, transducer performance can be improved by increasing the number of elements and increasing the interelement spacing to above half the wavelength. Interply spacing is important in beam steering accuracy.

CHAPTER 3

BACKGROUND

This section is intended to provide a background on composite materials, propagation characteristics of plate waves, and triangulation theory. The section begins with a background on the types of failure modes associate with composite materials and describes the two material systems used in this investigation. MAE is introduced by providing a background on the wave propagation characteristics of plate waves. The importance of phase velocity and phase points used to locate events are introduced and methods used to obtain them for the material systems under investigation. The section ends with background on traditional triangulation theory and how it is used to locate events using AE.

3.1 Material System

Composites are used in the aeronautic and aerospace industry due to their diverse applications. Composites have a much lower strength-to-density ratio than traditional metals thereby decreasing weight while retaining strength. Although composite materials cost more to manufacture, they can decrease weight, reduce fuel

costs, and open the door for a wide variety of manufacturing capabilities. While the benefits of composites outweigh their high cost, composite maintenance concerns must be addressed due to their complex failure modes.

Degradation of mechanical properties can be caused by, but not limited to, impact damage, mechanical loading, thermal fatigue, corrosive attack, wear, thermal dimensional stability, fatigue, and aging. In the aerospace industry, impact damage is a large area of concern due to the increased use of composites (1). Failure due to mechanical loading is localized in the fibers, matrix, or the fiber-matrix interface as well as a combination of all three. Failure in composites is attributed to initiation and propagation of multiple microscopic or individual macroscopic cracks and their shared interactions. The accumulation of cracks causes the degradation of the mechanical properties of the composite. This degradation leads to a loss of integrity and can result in failure of the composite (19). The types of damage modes induced during mechanical loading are matrix cracking, splitting cracks, delaminations, and fiber failure.

Two types of composite material systems have been studied in this investigation: 1) strength critical and 2) stiffness critical. Strength critical structures are designed to withstand large forces in the form of compression, tension, shear, and pressurization. Stiffness critical structures (typically honeycomb or foam sandwich composites), on the other hand, are designed to withstand bending stresses.

The MAE impact location techniques will be demonstrated on two full-scale composite components. Both components are cylindrical in shape and consist of graphite epoxy material systems provided by ATK Aerospace Corporation Aerospace

Structures division. The stiffness critical structure is a thin skin sandwich structure with an aluminum core and approximate dimensions of 90 inches in height and 130 inches in diameter with areas of complex geometries and multiple cutouts (see Figure 2). The structure's graphite epoxy skins are quasi-isotropic with a combined relative thickness of 12% to that of the aluminum core. The strength critical structure is a cylindrical laminate with approximate dimensions of 46 inches in diameter and 38 feet in height. The structure is a filament wound solid graphite epoxy balanced laminate of varying thickness with plies of two varying angles as well as a variable thickness liner (see Figure 3).

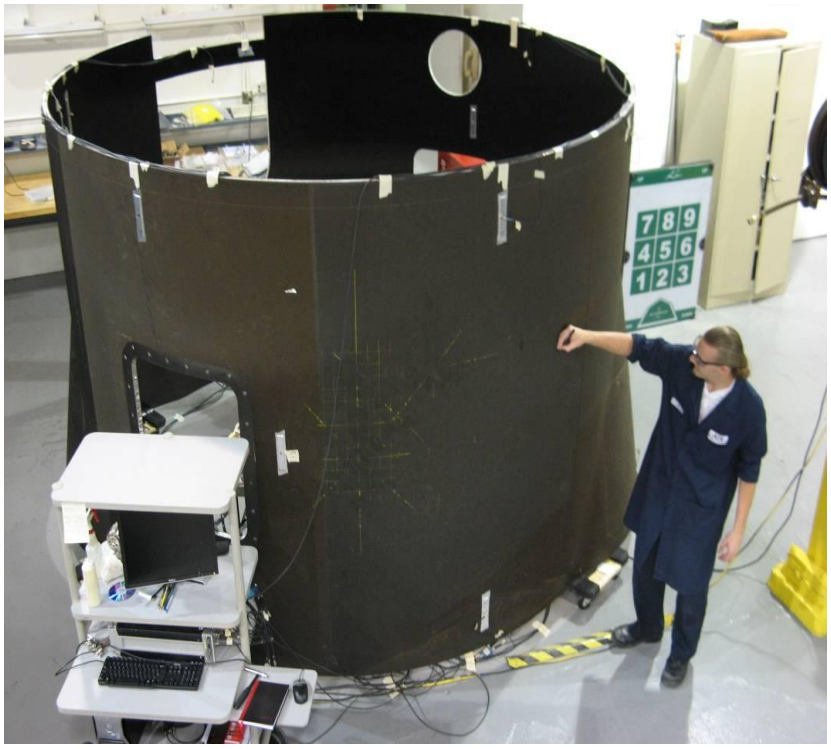

Figure 2. Stiffness critical structure used in this work.

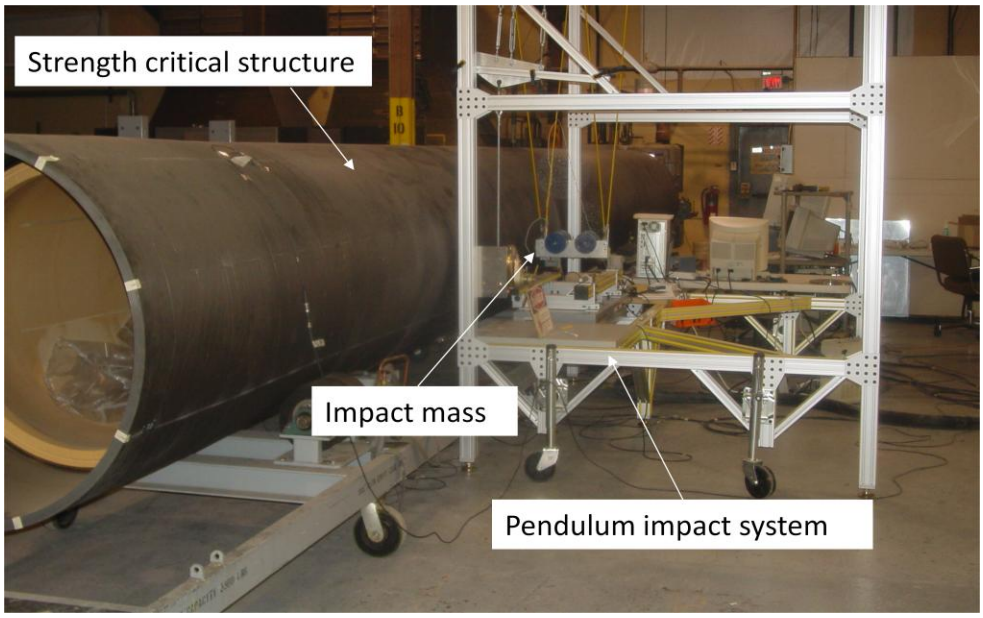

Figure 3. Strength critical structure alongside an impact pendulum system used to produce damage for material characterization.

3.2 Impact Damage and Detection

Impact damage in composites is an increasingly important issue in the aerospace industry due to increased use of composite components in space systems, aircraft, and air launch missiles. Unlike homogeneous materials, impacts on composites may not be visible on the surface and as a result, sophisticated techniques are needed to identify and characterize them (1). MAE provides a way to monitor a composite component for impact damage or strength-reducing events and to locate the source, resulting in a decrease in time out of service due to inspection time. Development of an MAE system that can monitor the structural health of a composite structure greatly reduces the cost and risk associated with maintenance, replacement of a component/subcomponent due to damage, and use of composites in aerospace and aircraft systems.

The impact detection system utilized in this investigation uses data obtained from the detection of strength-reducing events to locate the estimated source. The rapid release of energy due to a strength-reducing event results in the propagation of a guided plate wave due to the resulting deformation in the material system and the constraining boundary conditions. The induced Lamb wave is detected by piezoelectric sensors and is analyzed using specialized software to determine frequency content, amplitude, energy, and arrival time information that is used to back-calculate the estimated location of the event.

3.3 Modal Acoustic Emissions (MAE) Theory

Acoustic emissions are a type of elastic wave propagating in a solid due to the rapid release of energy. Sources of acoustic events can range from friction, crack initiation and propagation, and impact events. Modal AE differs from traditional AE by capturing the specific frequency components and modes in the propagating wave in order to characterize the type of event occurring and to more accurately locate the source. The following describes plate wave propagation characteristics and the critical characteristics of the wave required to accurately locate events on composite structures.

3.3.1 Lamb Waves

Lamb waves are a type of elastic wave that have been proven to have diverse applications in ultrasonic testing (5). Lamb waves are elastic displacements that

propagate in the transverse direction of a solid plate with traction-free boundaries created by bulk waves interacting with the stress-free surfaces of a plate (20). When the bulk wave contacts the surface, mode conversion occurs. The multiple reflections of bulk waves off the plate's surfaces constructively add up to form guided waves know as plate waves or "normal modes".

Using the wave equation for a solid and applying the stress-free boundary conditions, the displacements can be found that describe the true nature of Lamb waves. Consider a plate with thickness 2d where the z-axis is parallel to the surface normal and the x-axis is the direction of a propagating Lamb wave. According to the fundamental theorem of vector calculus (Helmholtz's theorem), the particle displacement vector, **V**, can be expressed by the divergence and the curl of two unknown functions, the scalar potential Φ and the vector potential $\boldsymbol{\psi}$, using the following equation:

$$\mathbf{V} = -\nabla\Phi + \nabla \times \boldsymbol{\psi} \qquad [1]$$

where Φ and ψ in this case are the displacement potentials for the longitudinal and shear waves of the vector field, respectively. The component of the vector potential in the y-axis will have a nonzero magnitude since wave motion does not depend on that axis. Therefore, the potentials must satisfy the time dependent form of the wave equation for a perfectly elastic solid:

$$\frac{\partial^2\Phi}{\partial x^2}+\frac{\partial^2\Phi}{\partial z^2}+k_l^2\Phi=0 \quad \& \quad \frac{\partial^2\psi}{\partial x^2}+\frac{\partial^2\psi}{\partial z^2}+k_t^2\psi=0 \qquad [2]$$

where $k_l=\omega\sqrt{\rho/(\lambda+2\mu)}$) and $k_t=\sqrt{\rho/\mu}$ are the wave numbers of the longitudinal and transverse modes, respectively. The remaining constants refer to the angular frequency ω, Lame's constants λ and μ, and the density of the medium ρ. The resulting stresses caused by the particle displacement components, denoted U and W, along the x and z axes can be related to the potentials using Hooke's law and the strain displacement equations for an isotropic homogenous material as follows:

$$U=\frac{\partial\Phi}{\partial x}-\frac{\partial\psi}{\partial z} \quad \& \quad W=\frac{\partial\Phi}{\partial z}+\frac{\partial\psi}{\partial x} \qquad [3]$$

$$\sigma_{xx}=\lambda\left(\frac{\partial^2\Phi}{\partial x^2}+\frac{\partial^2\Phi}{\partial z^2}\right)+2\mu\left(\frac{\partial^2\Phi}{\partial x^2}-\frac{\partial^2\psi}{\partial x\,\partial z}\right),$$

$$\sigma_{zz}=\lambda\left(\frac{\partial^2\Phi}{\partial x^2}+\frac{\partial^2\Phi}{\partial z^2}\right)+2\mu\left(\frac{\partial^2\Phi}{\partial z^2}-\frac{\partial^2\psi}{\partial x\,\partial z}\right),$$

$$\sigma_{xz}=\mu\left(2\frac{\partial^2\Phi}{\partial x\,\partial z}+\frac{\partial^2\psi}{\partial x^2}-\frac{\partial^2\psi}{\partial z^2}\right) \qquad [4]$$

Viktorov (5) gives the following solutions for Φ and ψ with arbitrary constants A_S, B_A, D_S, and C_A:

$$\Phi=A_s\cos(qz)e^{ikx}+B_a\sin(qz)e^{ikx}$$

$$\psi = D_s \sin(sz) e^{ikx} + C_a \cos(sz) e^{ikx} \quad [5]$$

where $q = \sqrt{k^2 - k_l^2}$; $s = \sqrt{k^2 - k_t^2}$; and K is the Lamb wave number. The importance of the subscripts s and a will be seen later. Note that the time-dependent factor $e^{-i\omega t}$ has been left out; however, this term should be included if the displacement component as a function of time is to be explored. The given solutions satisfy the wave equations given in Equation 2. Substituting these equations into the stress equations given in Equation 4 and using the boundary conditions that σ_{XZ} and σ_{ZZ} equal zero at the plate's edges (z = ±d), a linear system of four homogeneous equations can be found and used to solve for the four arbitrary constants. Using linear algebra, the equations can be further reduced to two characteristic equations that describe the dispersion characteristics of Lamb waves utilizing the fact that the system has nontrivial solutions when there determinates are zero, as will be discussed in the next section. For a full derivation, refer to Viktorov (5). By determining the eigenvalues of the Lamb wave number k, the four constants can be reduced to two and the following equations are found for the potentials:

$$\Phi = A_s \cos(q_s z) e^{ik_s x} + B_a \sin(q_a z) e^{ik_a x}$$

$$\psi = \frac{2ik_s q_s \cos(q_s d)}{(k_s^2 + s_s^2)\sin(s_s d)} A_s \sin(s_s z) e^{ik_s x} + \frac{2ik_a q_a \cos(q_a d)}{(k_a^2 + s_a^2)\sin(s_a d)} B_a \cos(s_a z) e^{ik_a x} \quad [6]$$

where $q_{s,a} = \sqrt{k_{s.a}^2 - k_l^2}$, $s_{s,a} = \sqrt{k_{s.a}^2 - k_t^2}$, and k_s and k_a are the k values satisfying the four linear homogeneous equations. The displacement components U and W can then be found by substituting Equation 6 into Equation 3 and using superposition:

$$U = U_s + U_a \quad \& \quad W = W_s + W_a \qquad [7]$$

It is seen from the superposition of the displacement components that there are two groups of waves satisfying the wave equation in motion and in boundary conditions and propagate independently of one another. The two groups of waves are separated by the subscripts s and a. The subscript s refers to waves that propagate symmetrically with respect to the center of the plate and are therefore referred to as symmetrical Lamb waves or "extensional" waves. The second wave type, subscript a, refers to wave motion that is antisymmetrical with respect to the plates midline and is known as the antisymmetrical Lamb wave or "flexural" wave. A representation of both can be seen in Figure 4. The extensional and flexural waves are two out of the three distinct types of guided waves with traction free boundaries. The third wave has only displacements in the plane of the plate; known as a horizontally polarized shear wave (Love wave). These waves are not of interest for the purposes of this work.

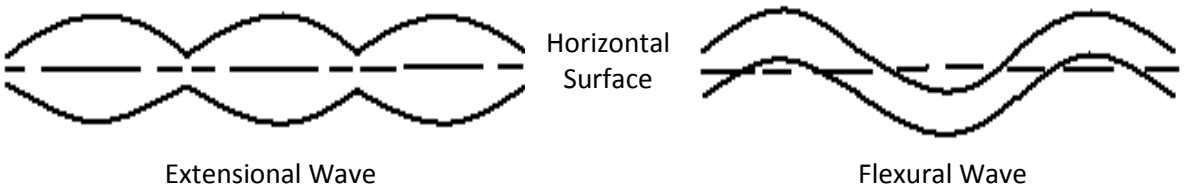

Figure 4. Flexural and Extension Wave mode.

3.3.2 Dispersion and Wave Speed Characteristics of Lamb Waves

The displacements of the two propagating waves are not of importance for the purposes of this thesis and are therefore left out. What is important is the propagation characteristics of the Lamb wave modes: there dispersion characteristics and resulting velocities. As stated in the previous section, the four linear homogeneous equations were reduced to two characteristic equations given by the following:

$$(k^2 + s^2)^2 \cos(qd) \sin(sd) - 4k^2 qs \sin(qd) \cos(sd) = 0;$$

$$(k^2 + s^2)^2 sin(qd) cos(sd) - 4k^2 qs\, cos(qd)\, sin(sd) = 0 \qquad [8]$$

Each root defines a characteristic wave with a specific wave number $k_{s,a}$. As seen when solving for k, there are an infinite number of solutions for the flexural and extensional waves for a given frequency. The number of wave modes present is dependent on the medium supporting the waves as well as the frequency of the waves themselves. Some solutions to the characteristic equation will result in complex

solutions which correspond to in-phase motions of the plate. These imaginary solutions decay or grow exponentially along the plane of motion within the plate and therefore are not considered in this study. It is only the real solutions of the characteristic equations which result in the types of waves of interest. Each real root found corresponds to a mode and since there are two independently propagating waves, each root results in one mode for each type of wave.

If ωd, angular frequency multiplied by the plate thickness, approaches zero and Equation 8 is solved, only one real root will be found which is designated the zeroth symmetrical (S_0) and antisymmetrical (A_0) modes. The roots k_{s_0} and k_{a_0} as ωd is increased will change in size relative to one another. At specific ratios between ω and d, new roots will appear which comprise the first, second, third, and higher Lamb wave modes. The specific ratios of ω and d that result in new modes are referred to as the critical thicknesses and frequencies. Guided waves can only exist for the specific combinations of frequency and thickness that result in a standing wave in the thickness direction. The relationship between the longitudinal and transverse waves (bulk waves) and the critical thickness resulting in standing waves are given for the symmetrical (extensional) modes as shown in Equation 9 (5):

$$2d = \frac{\lambda_l}{2}, \frac{3\lambda_l}{2}, \frac{5\lambda_l}{2}, \dots;$$

$$2d = \lambda_t, 2\lambda_t, 3\lambda_t, \dots \quad [9]$$

and are given for the antisymmetrical (flexural) modes as Equation 10 (5):

$$2d = \lambda_l, 2\lambda_l, 3\lambda_l, \ldots;$$
$$2d = \frac{\lambda_t}{2}, \frac{3\lambda_t}{2}, \frac{5\lambda_t}{2}, \ldots \quad [10]$$

When a new standing longitudinal or transverse wave is generated, at the critical frequencies, the wave numbers $k_{s,a} \rightarrow 0$ while the phase velocities $c_{s,a} \rightarrow \infty$.

The fundamental characteristic of a Lamb wave is its phase velocity (5). The phase velocity is the one characteristic that differentiates each mode from one another and once it is found, the wave number can be determined and the stresses and displacements in the plate calculated. Numerical solutions to the characteristic equations lead to solutions for the phase velocity which are given for an isotropic plate by the Rayleigh-Lamb dispersion relations for the symmetric (extensional) modes (8):

$$\frac{\tan \beta\frac{d}{2}}{\tan \alpha\frac{d}{2}} = -\frac{4\alpha\beta k^2}{(k^2-\beta^2)^2} \quad [11]$$

and for the antisymmetric (flexural) modes:

$$\frac{\tan \beta\frac{d}{2}}{\tan \alpha\frac{d}{2}} = -\frac{(k^2-\beta^2)^2}{4\alpha\beta k^2} \quad [12]$$

where α and β are:

$$\alpha^2 = \frac{\omega^2}{C_l^2} - k^2$$

$$\beta^2 = \frac{\omega^2}{C_t^2} - k^2 \qquad [13]$$

where $k = \omega/c$, $\omega = 2\pi f$ is the angular frequency, c the Lamb wave phase velocity, C_l the longitudinal wave velocity, and C_t the transverse (shear) wave velocity. Closed formed expressions to these equations do not exist; therefore, solutions must be found numerically. The reader is referred to Rogers (8) for more simplified equations for numerical solutions. The Rayleigh-Lamb equations are referred to as the dispersion curves due to their dependence on frequency. Guided plate waves are dispersive in nature, meaning that there phase velocities are dependent on frequency (21). The dispersion relationships are different for each mode as can be seen in Figure 5 and 6 and are dependent on the elastic properties, bulk wave velocities, and the thickness of the medium.

All propagating waves (acoustic, electromagnetic, etc.) consist of a collection of individual waves with different frequencies and wavelengths known as a wave packet (22). The interactions of these individual waves shape and define the structure of the wave packet as it propagates in time. Therefore, within a propagating wave, there are two types of wave speeds that must be considered: 1) the group and 2) the phase

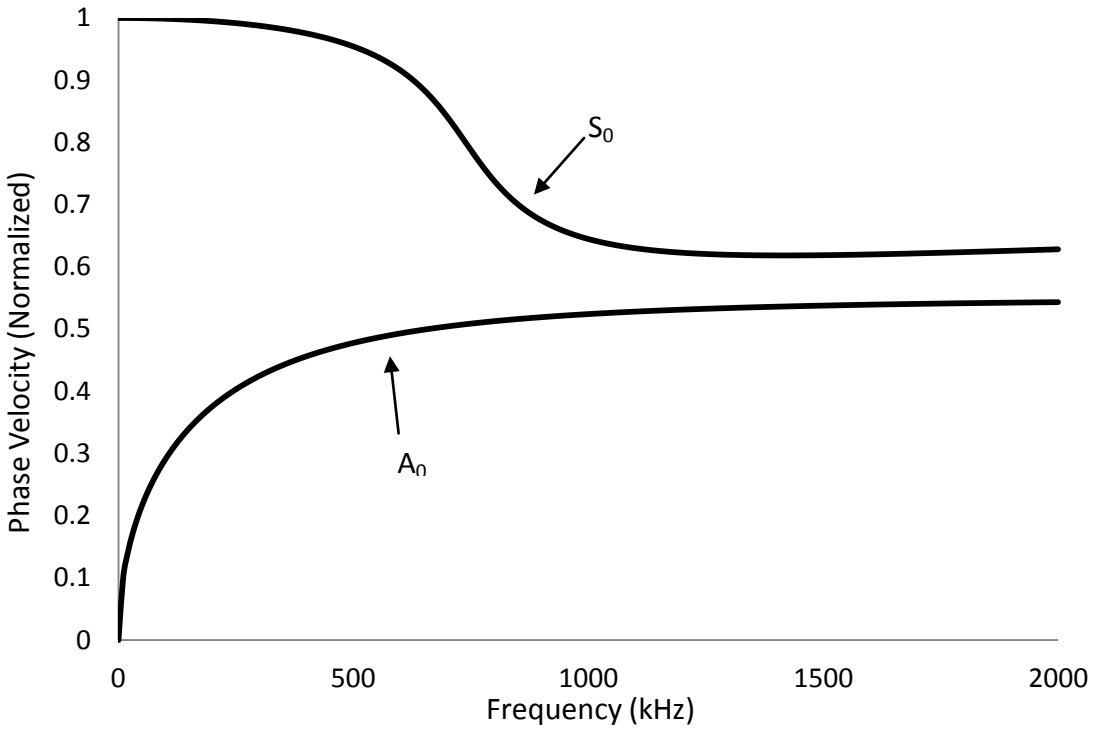

Figure 5. Normalized plot showing the dispersion curves for the first symmetric (S_0) and antisymmetric (A_0) phase velocities in a quarter inch thick aluminum plate.

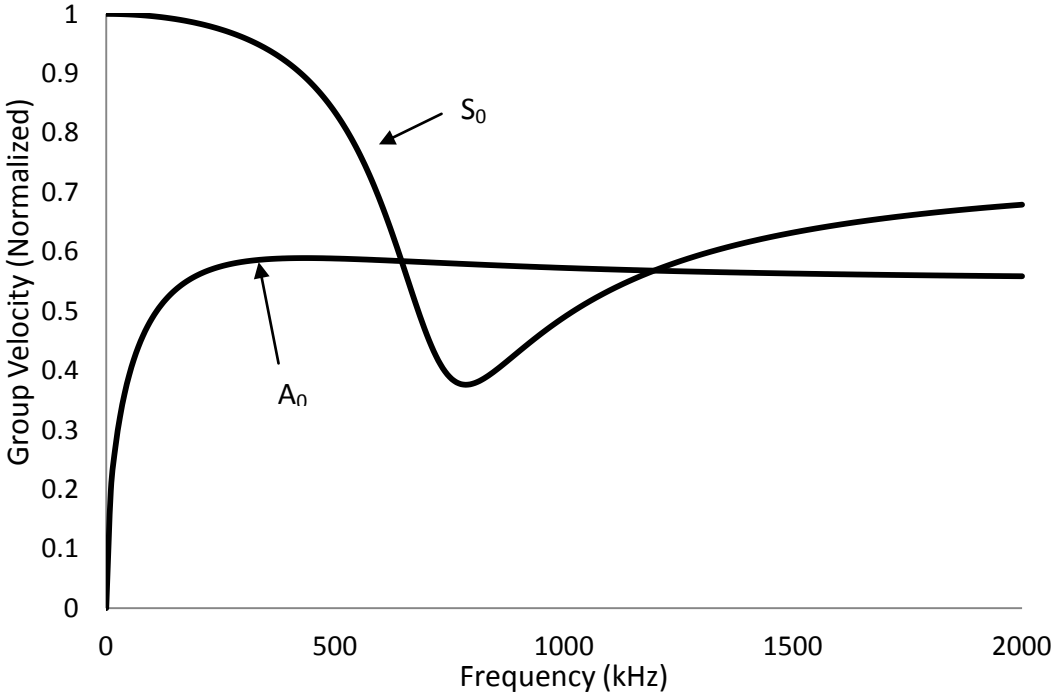

Figure 6. Normalized plot showing the dispersion curves of the first symmetric (S_0) and antisymmetric (A_0) group velocities in a quarter inch thick aluminum plate.

velocities. The group velocity is the velocity at which the envelope of the wave packet itself propagates and the phase velocity is the speed at which a particular frequency component within the wave packet itself propagates and as such, the group velocity is dependent on the phase velocities.

Using the Rayleigh-Lamb dispersion relations, the phase velocity and therefore the group velocity can be found. However, upon inspection of the Rayleigh-Lamb equations, an even more complicated nature of Lamb wave velocities for use in anisotropic materials can be seen. Lamb wave phase velocities are dependent on the longitudinal and transverse wave bulk wave velocities in an isotropic medium by Equation 14:

$$C_l = \sqrt{\frac{E}{\rho}\frac{(1+\upsilon)}{(1+\upsilon)(1-2\upsilon)}}$$

$$C_t = \sqrt{\frac{E}{\rho}\frac{1}{2(1+\upsilon)}} \qquad [14]$$

Notice for an isotropic medium that the bulk wave velocities (longitudinal and transverse wave speeds) and therefore the Lamb wave velocities are directly dependant on the square root of Young's modulus. In anisotropic materials such as composites, however, Young's modulus is orientation-dependent and therefore, velocities are orientation-dependent, as can be seen in Figure 7. This means that the Lamb waves under investigation for impact detection and locating will change velocities with

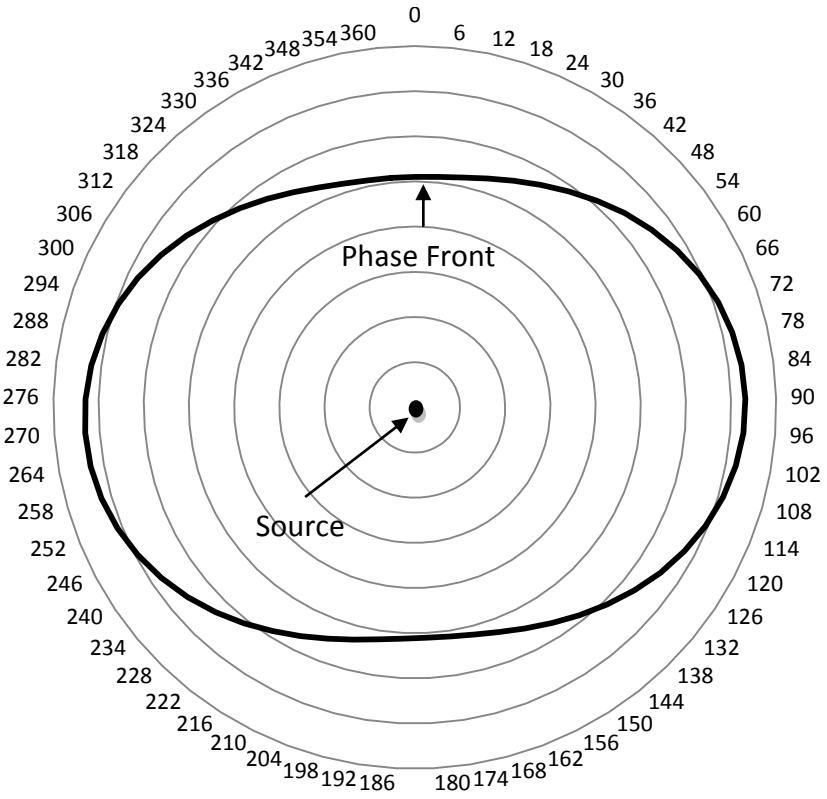

Figure 7. Radial plot showing the anisotropic nature of a wave propagating in time from a point of impact as a function of orientation in a composite material.

different propagation directions as well as for different frequency components, further complicating the methods of locating impacts from arrival time information.

In a dispersive medium, the individual waves making up the wave packet will propagate with different wave speeds; therefore, the shape of the wave packet will change as the wave propagates (22). This implies that locating by use of the group velocity can result in large errors. By isolating a specific frequency component within the wave packet, dispersion effects can be neglected. As such, it is important to use the phase velocity for source location and not the group velocity in dispersive mediums.

To increase the accuracy of event locating in a given material system, the phase velocity profile should be determined and built into the location algorithms. Before determining the phase velocity profile, a frequency must be chosen in which the profile will be determined for. The frequency chosen should be that in which the combination of both the material and the detection system are most responsive. By selecting the most responsive frequency of the material/detection system, variations in the wave speed used to locate the source can be minimized to orientation only dependent wave speeds and dispersion neglected.

3.3.3 Phase Velocity Profile

Theoretical determination of Lamb wave phase velocities in composite materials is complicated by the anisotropy, dispersion, local to global material changes, and manufacturing variability. Therefore, it was found that a method is needed to determine the wave speed profile experimentally. Each composite material system has its own characteristic phase velocity profile and dispersion curve as seen in the Rayleigh-Lamb dispersion relations. Phase velocity profiles must be determined for each material system so that the appropriate location algorithm can be developed according to the profile.

Phase velocity was found by exciting the medium with a sine wave using a function generator centered at a single frequency at a given burst rate using a fixed position pulsing sensor. Using a receiving sensor, the phase velocity can be found by tracking a chosen phase point within the wave packet by moving the receiving sensor a

known distance and determining the time of flight. Doing this for various directions, a velocity profile can be determined for the chosen frequency by fitting the data to a trigonometric or polynomial function. Figure 8 shows one such velocity profile for a 10 kHz excited sine wave performed on the stiffness critical structure. Doing this for each frequency, the experimental phase velocity dispersion curves can be generated for a given direction.

Material systems investigated in this study are quasi-isotropic in nature. In most cases, the velocity profile will exhibit symmetries similar to that of trigonometric functions. In Figure 8, the velocity profile matches a cosine wave as it will for most quasi-isotropic material systems. It is proposed then that the phase velocity data obtained experimentally can be fit to the following equation:

$$C_f(\theta) = A\cos(\omega\theta + \phi) + B \qquad [15]$$

where A is the amplitude of the fit equation related to the spread in the velocity data points, ϕ is the phase shift of the cosine wave to fit the data, B is the vertical shift, and ω is the angular frequency related to the number of periods. Note that the subscript *f* implies frequency dependence. The cosine function is used as opposed to the sine function for reasons seen later in the phased array location techniques section. Using this equation, the velocity profiles of most material systems can be determined as a function of orientation.

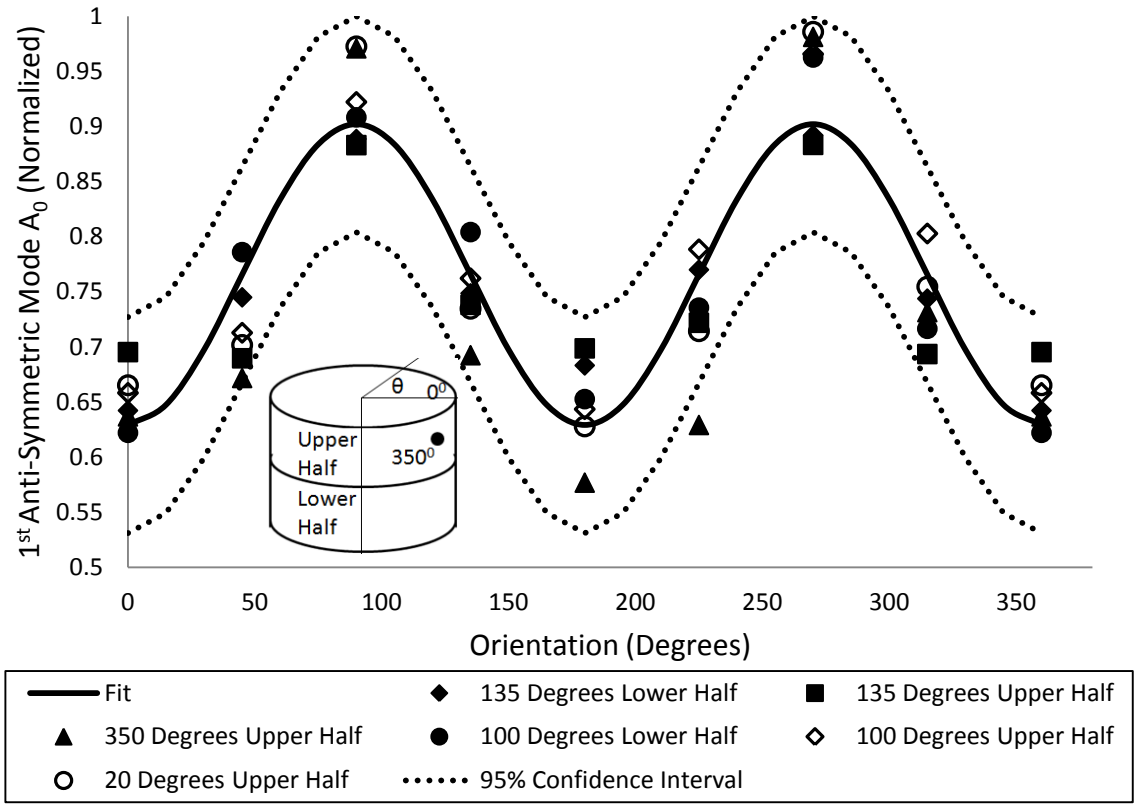

Figure 8. Velocity profile fit from phase velocity measurements made on the stiffness critical structure excited at 10 kHz by a sine wave using a function generator. The velocity profile was found experimentally at various locations along the outer circumference of the stiffness critical structure and the results used to fit a general velocity profile.

3.3.4 Phase Points

In order to accurately locate events, accurate arrival time information from sensor to sensor of the propagating wave must be identified. To eliminate effects due to dispersion, it was shown that the phase velocity must be used to calculate the location of an event and as such, the arrival times must be determined by tracking the same phase point from sensor to sensor. However, due to dispersion and attenuation, locating the same phase point from sensor to sensor can be a difficult task since the

shape of the wave will change as it propagates. In order to reduce these effects, techniques derived from the method of phased array technology should be utilized.

Utilizing phased array techniques, phase points can be identified from sensor to sensor much easier, as can be seen in Figure 9. In phased array, multiple sensors are placed side by side and utilized as a single element to increase scan times and resolution. If the MAE sensors are arranged in a similar fashion, the same phase point from sensor to sensor can be tracked with greater accuracy. The spacing between each sensor is directly related to the wavelength of the propagating wave. The sensor spacing should be smaller than the length it takes the wave to travel one half cycle so that the phase point can be accurately tracked. Using the phase velocity of a particular frequency component in conjunction with phased array techniques allows for more accurate arrival time information, leading to greater accuracy in the estimated source location.

3.4 Triangulation Theory

Impact detection systems currently in use typically utilize triangulation techniques to locate the source of strength-reducing events (4). Triangulation is the method of determining the location of a point by using distances between known points and the angle from these known points to the location under investigation. For impact detection using AE, however, the angles from the known sensor locations to the source of the event are unknown. Using basic trigonometric relationships and the relationship between time, distance, and velocity, a system of equations can be derived to

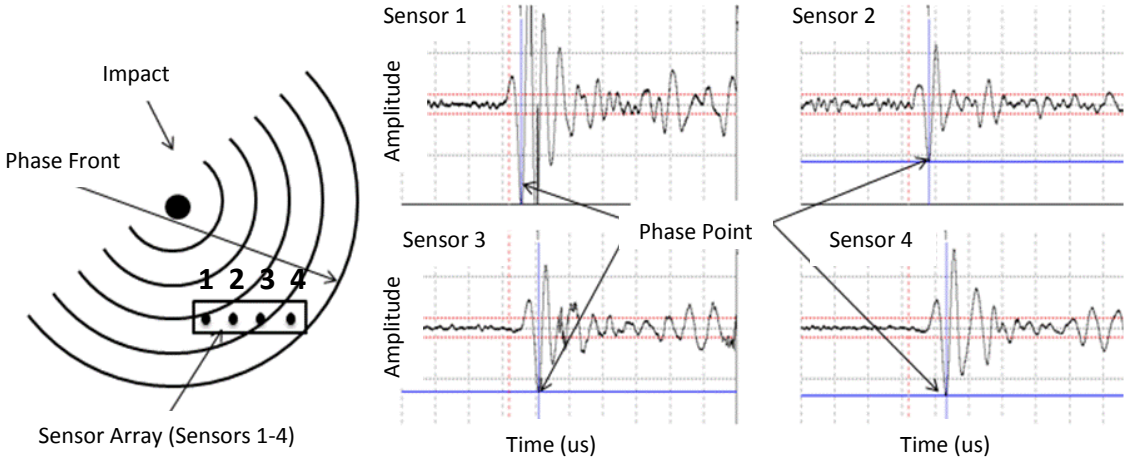

Figure 9. Schematic demonstrating how the use of linear phased array techniques can be used to determine the same phase points from sensor to sensor for more accurate arrival time information.

triangulate the source. There are two main types of triangulation: one-dimensional and two-dimensional triangulation which are discussed in the following.

3.4.1 One-Dimensional Triangulation

One-dimensional triangulation utilizes the relationship between velocity, distance, and time to determine the location of an event. For two sensors separated a distance D from one another, two simple equations can be found relating the vertical distance to the impact location from the first sensor (see Figure 10).

The two equations relating the sensor spacing and impact location are given by Equation 16:

$$x = v * t_1$$

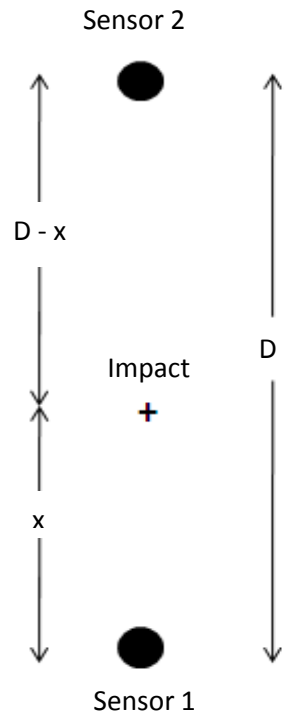

Figure 10. Schematic diagram describing 1-D triangulation theory.

$$D - x = v * t_2 \quad [16]$$

where v is the wave speed in the given material system and t_1 and t_2 are the times of flight from impact to each sensor, respectively. However, it should be noted that time of flight information is unknown when using acoustic emissions. Only the relative arrival times between each sensor are known relative to the arrival time recorded at the first sensor in which the propagating wave passes. When the propagating wave passes the first sensor in the system, it initiates the system to begin recording. Assuming that the length of the window is long enough, each sensor will then record the wave as it passes. Therefore, the difference in arrival times can be determined as follows:

$$\Delta T = t_{i+1} - t_i \quad \text{Where } i\text{= 1, 2, 3, . . , N} \qquad [17]$$

where N is the total number of sensors in the system. By subtracting the two equations from one another, the distance between the sensors to impact can be found by solving for the unknown variable:

$$x = \frac{D - v * \Delta T}{2} \qquad [18]$$

3.4.2 Two-Dimensional Triangulation Theory

Two-dimensional triangulation theory was first developed by Tobias in 1976 (4). The following gives a quick derivation of the formula but the reader is referred to reference (4) for a more in-depth understanding. The solution is found by relating the equation of a circle to the velocity in the material system and the arrival time data for each sensor in the system. A circle encompassing each sensor whose radius is equal to the distance from the sensor to the actual point of impact represents all possible locations where the source of the impact may be located (see Figure 11).

When three or more sensors are combined, the points of intersection correspond to the point of estimated impact. For a system of three sensors, the three equations for the circles are given by:

$$x^2 + y^2 = r^2 \qquad [19]$$

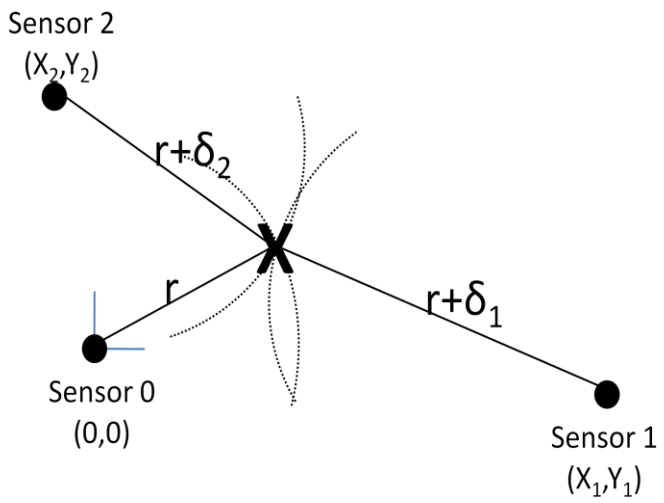

Figure 11. Schematic of 2-D triangulation based on the Tobias Model.

$$(x - x_1)^2 + (y - y_1)^2 = (r - \delta_1)^2 \quad [20]$$

$$(x - x_2)^2 + (y - y_2)^2 = (r - \delta_2)^2 \quad [21]$$

where:

$$\delta_1 = v * (t_1 - t_0) \quad [22]$$

$$\delta_2 = v * (t_2 - t_0) \quad [23]$$

A solution can then be found by expanding Equations 20 and 21 and subtracting Equation 19 from each respectively. The remaining two equations are then equated to one other, converted to polar coordinates, and an equation for r is determined. Then, through a series of mathematical manipulations, the following solution is found:

$$\theta = \phi + \beta$$

$$x = r\cos\theta \quad \& \quad y = r\sin\theta \qquad [24]$$

where:

$$\tan\phi = \frac{(A_1 y_2 - A_2 y_1)}{(A_1 x_2 - A_2 x_1)}$$

$$\beta = \cos^{-1}|k|$$

$$k = \frac{(A_2\delta_1 - A_1\delta_2)}{B}$$

$$B = [(A_1 x_2 - A_2 x_1)^2 + (A_1 y_2 - A_2 y_1)^2]^{1/2}$$

$$A_1 = x_1^2 + y_1^2 - \delta_1^2 \qquad \& \qquad A_2 = x_2^2 + y_2^2 - \delta_2^2$$

$$r = \frac{A_1}{2(x_1\cos\theta + y_1\sin\theta + \delta_1)} = \frac{A_2}{2(x_2\cos\theta + y_2\sin\theta + \delta_2)} \qquad [25]$$

3.4.3 Triangulation Accuracy

For isotropic material systems, both methods of triangulation work well with relatively small errors. However, for complex material systems such as composites, the errors are greatly increased. The cause for such large errors is attributed to the velocity. Triangulation methods are based on constant wave speeds and not orientation-dependent wave speeds that occur in anisotropic material systems. Solutions to both triangulation equations become too complicated to solve explicitly and numerical solutions are time consuming.

Another source of inaccuracy is found when this method is applied to large structures. The Tobias 2-D location method works well when the impact is located inside the sensor configuration; however, it begins to fail with increasing distance outside of the sensor configuration. To apply this method to large structures, the sensors must be placed at large distances from one another or a large sensor density should be utilized.

Two 2x2 foot plates were used to compare the 2-D location method for two basic types of material systems: isotropic and anisotropic. The isotropic plate was made of aluminum a quarter inch in thickness and the anisotropic plate, a quasi-isotropic graphite/epoxy material approximately a sixteenth of an inch in thickness. Figure 12 shows the results of the estimated locations of five impacts made at identical locations on both plates using the Tobias method where two of the impacts are outside of the configuration. For both plates the same sensors, equipment, and procedures were used for detection of the events and back-calculation of the source. Note that the error in the estimated distance to the source increases as the impact location increases in distance from the sensors configuration. Also note that for the composite plate, the error increases greatly with distance due to the inaccuracy in using the proper orientation dependent wave speed as well as the correct phase points as was discussed in Section 3.3.4.

It can be seen that a new method needs to be derived that includes anisotropic wave speeds to increase the accuracy of locating the source of events in large composite structures while decreasing the sensor density. As was shown, utilizing phased array techniques allows easier tracking of phase points and as will be seen, can incorporate

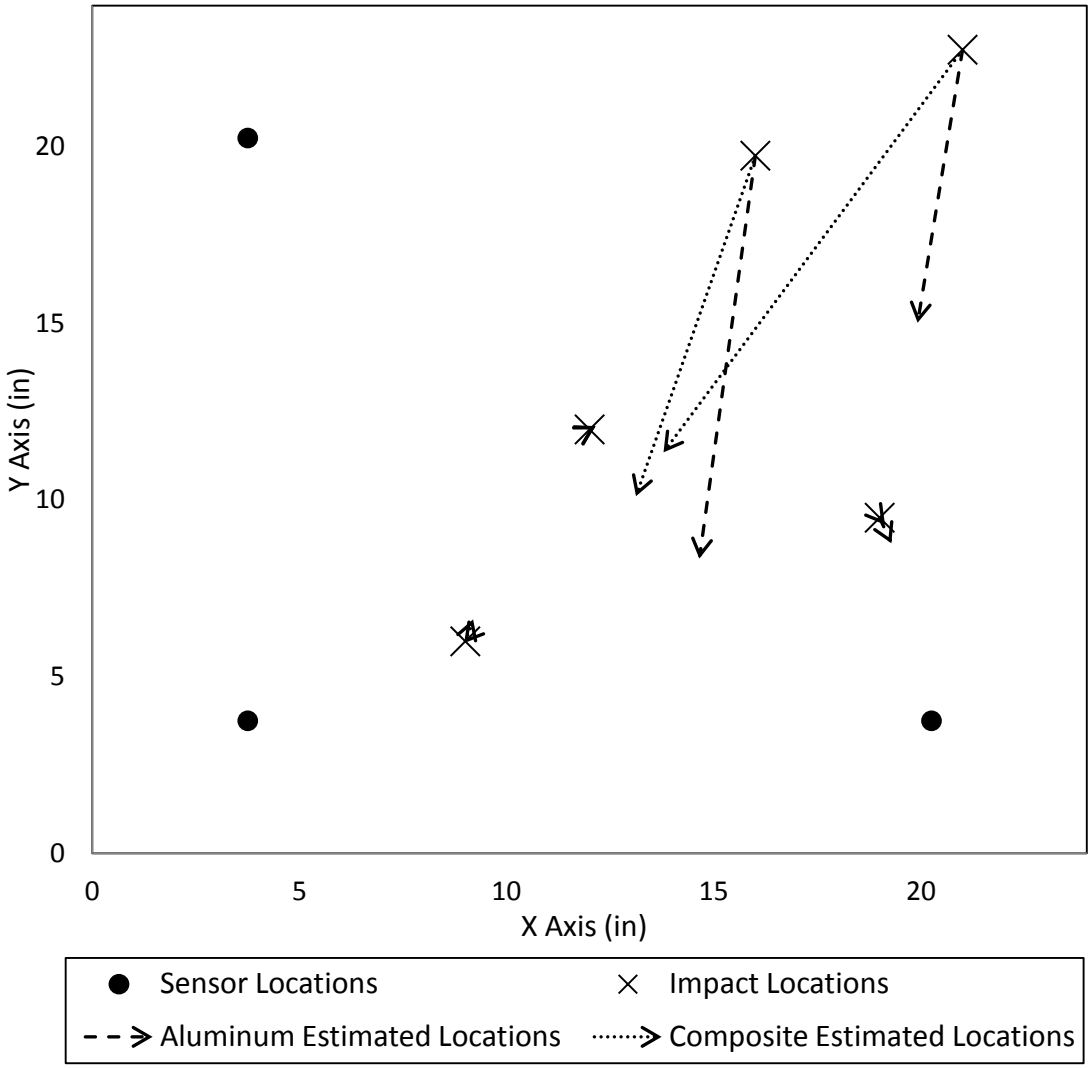

Figure 12. Estimated locations of five impacts performed on two 2'x2' panels made of 1) aluminum a 1/4" in thickness and 2) a graphite/epoxy plate 1/16" in thickness.

anisotropic wave speeds much easier than triangulation techniques. As such, the use of phased array techniques is explored in this work to increase event location accuracy and decrease the sensor/cabling requirements.

CHAPTER 4

PHASED ARRAY THEORY AND LOCATION ALGORITHMS

Phased array operates by manipulating a series of sensors to act as a single transducer to decrease inspection times and increase resolution. Phased array techniques have been adopted in this research to increase the accuracy of source location in anisotropic materials. Phased array methods utilize distances from a point of interest to each element within the array to determine the required timing sequence necessary to pulse each element to generate a focused wave at the point of interest. Here, the inverse method is used where arrival time information recorded at the array of sensors is coupled with the sensor spacing to back-calculate the estimated location of the source.

4.1 Background

Phased array systems are used to decrease inspection time and increase scan resolution by utilizing an array of elements combined into a single transducer (17). By varying the timing sequence of the excitation pulse for each element within the array, two types of imaging modes can be employed: 1) beam steering and 2) beam focusing.

For a linear array, beam steering operates by linearly varying the excitation pulse within each element in the array. The linearly varying time sequence results in N number of waves (for N sensors) that constructively add up resulting in a linear wave front of high amplitude in a given direction (see Figure 13). The change in timing sequence from sensor to sensor is directly related to the angle at which the beam is steered. Beam focusing, on the other hand, utilizes a spherical timing sequence that results in a wave front that converges at a specified point of interest (Figure 13). The point at which the waves converge is directly related to the spherical timing sequence used to excite the elements in the linear array.

The phased array time delay laws are needed in order to steer and focus a bulk wave at a predetermined point using known distances from the array to the location in

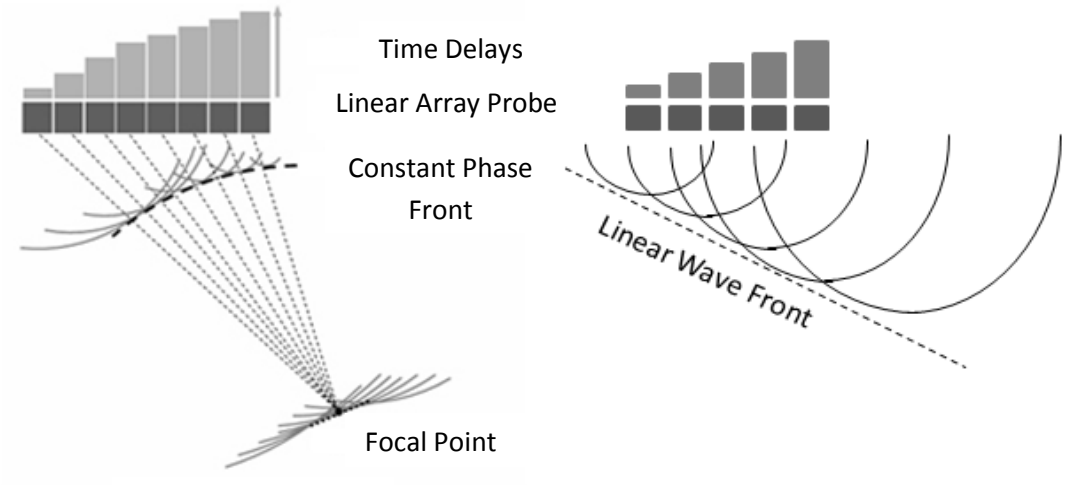

Figure 13. Schematic indicating how the phased array time delay laws are used steer and focus a beam formed by constructive interference.[2]

[2] Schematic of phased array beam focusing delay laws were provided by Bercli.

question. The required firing sequence for each element in the array to obtain constructive interference and convergence of the wave front at the desired point, O, can be derived using Figure 14. The time delay laws are given as follow (23):

$$\Delta t_n = \Delta t_n^s + \Delta t_n^f \quad [26]$$

where the contribution required to steer the beam is given by:

$$\Delta t_n^s = \frac{x_n \sin[\phi]}{v} \quad [27]$$

and the contribution required to focus the beam at the point O is:

$$\Delta t_n^f = -\frac{x_n^2}{2vr} \quad [28]$$

Note that the time delay law for beam steering is independent of distance and is only a function of the individual element's distance to the array center (x_n), the bulk wave velocity (v), and the angle from the normal of the array to the point in question (ϕ). Beam focusing, however, is a function of the distance from the array to the focal point O, the sensor spacing x_n, and the velocity of the propagating wave.

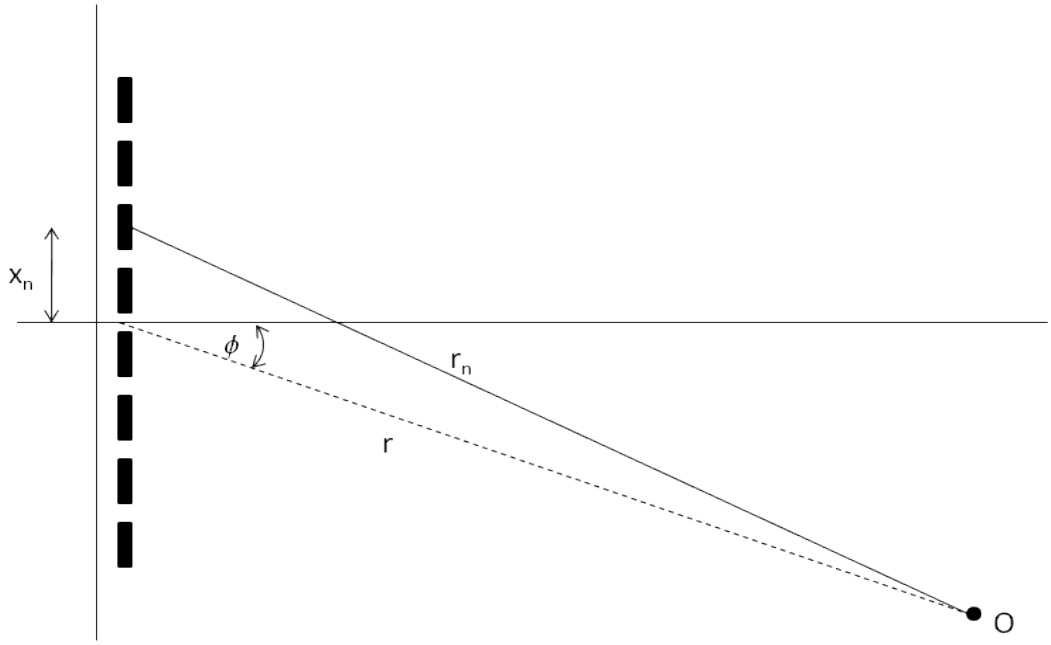

Figure 14. Schematic diagram indicating the geometry used to derive the phased array time delay laws for beam steering and focusing to a point O.

Using similar concepts, the inverse problem is undertaken in this work to determine the source of an event on a composite structure using the arrival times determined from a similar type of linear array based on acoustic emissions. As was described earlier, the only known values are the arrival time information and the locations of the sensors in the array. For this inverse phased array technique, the arrival times are used as the timing sequence coupled with the sensor spacing to back-calculate the estimated angle from the array to the source. Using a minimum of two arrays, the location of the source is estimated by determining the intersection of the beams extending from each array, as seen in Figure 15, for the case of beam steering. The techniques described in the following sections have been developed in cooperation with

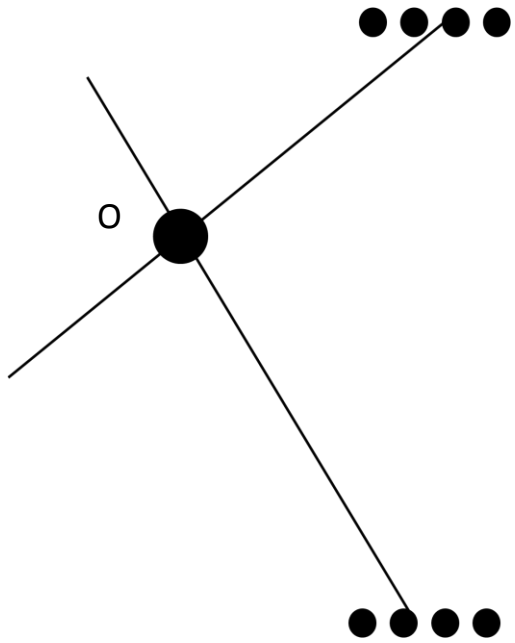

Figure 15. Beam steering schematic using two linear acoustical phased arrays to locate the estimated source, point O.

ATK and Digital Wave Corporation. It is of note that none of these techniques has been discussed in the open literature.

4.2 Quasi-Isotropic Beam Steering Algorithm

Phased array beam steering algorithms manipulate multiple elements in an array to act as a single transducer. For this investigation, multiple acoustic sensors are placed in a linear array and arrival time information along with sensor spacing is manipulated to act as a single sensor, resulting in the formation of a beam extending from the array center in the direction of the estimated source. When two or more arrays are set up in strategic locations, beams are steered from the array centers and intersect at the estimated location of the source, as was shown in Figure 15.

For the impact detection system developed in this investigation, four sensors are used per array. Each sensor is spaced a set distance α from one another. The sensor spacing must be smaller than one half the wavelength of the propagating phase front so that a particular phase point within the propagating wave can be tracked (see Figure 9):

$$\alpha < \frac{1}{2}\lambda \qquad [29]$$

Figure 16 provides a graphical representation of the inverse phased array method for impact detection. For the method to hold, the angle from each sensor to the source must be approximately equal to θ, meaning that the sensor spacing must be much smaller than the distance of the array to the source. Derivation of the solution depends on the type of material system on which the detection system is implemented: 1) isotropic and 2) anisotropic mediums. The following two sections describe how the algorithm is derived.

4.2.1 Isotropic Case

For isotropic materials, the elastic properties are assumed constant in all directions. Therefore, the phase velocity as a function of orientation is assumed constant. This leads to the assumption that the difference in arrival times from sensor to sensor is different by a linear factor, δ, if a linear array is used. This assumption is

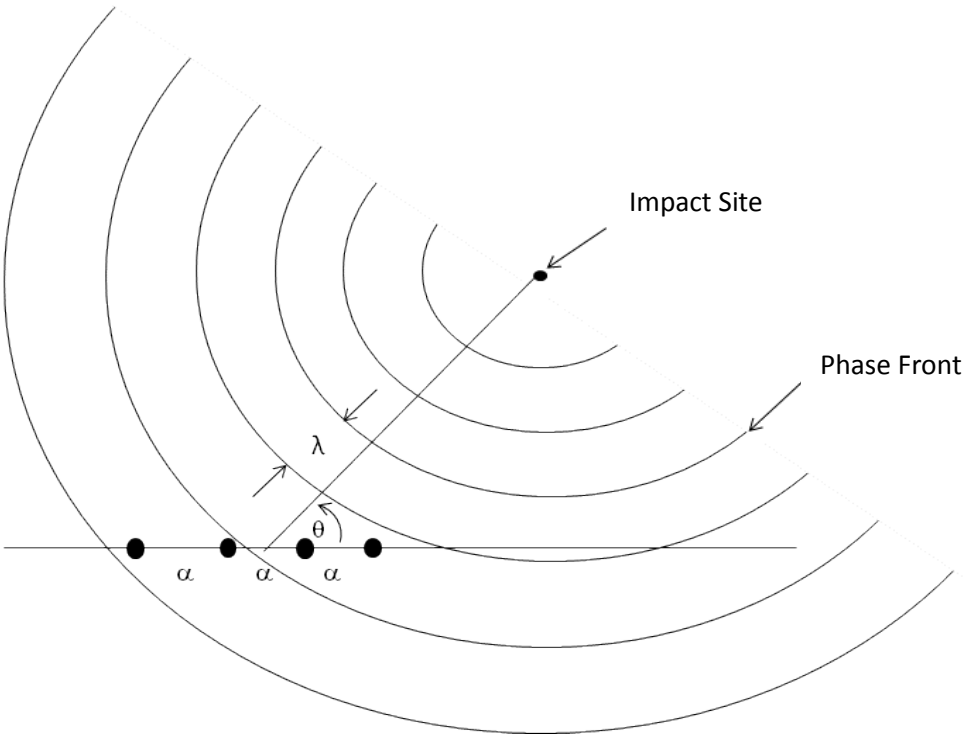

Figure 16. Graphical representation of the inverse phased array method for impact detection using beam steering.

supported by the phased array beam steering time delay law of linear sequential excitation pulses (see Equation 27). For an array consisting of N sensors, the relationship between the arrival times from sensor to sensor by definition then must be equal to δ divided by the velocity of the propagating wave:

$$\Delta T_{i,i+1} = \frac{\delta_\theta}{v_f} \quad [30]$$

Where ΔT is the difference in the arrival times of sequential sensors in the array, v is a

function of frequency, and δ depends on the orientation from the array at which the event occurs.

Using Figure 16 and the assumption of a linear shift in arrival times between sensors, a graphical representation of the quasi-isotropic beam steering method can be easily identified and used to derive the solution (see Figure 17). Using basic trigonometry, an equation relating θ to α and δ can be found, given as follows:

$$\cos\theta = \frac{\delta}{\alpha} = \frac{v_f * \Delta T}{\alpha} \quad [31]$$

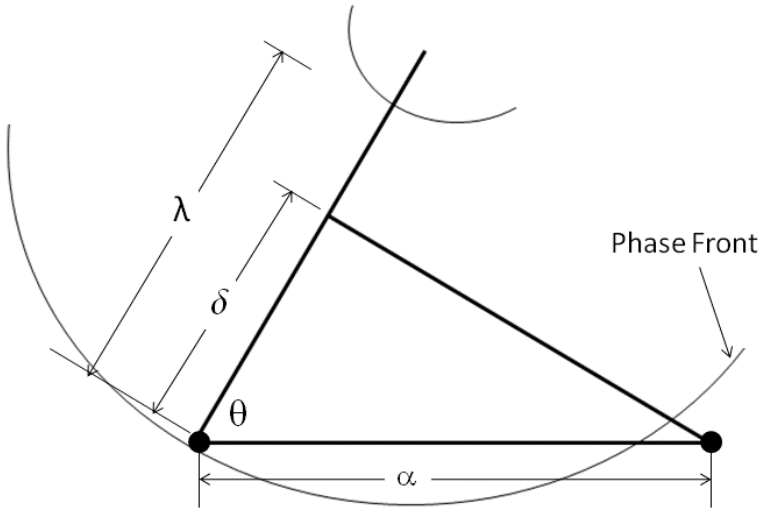

Figure 17. Graphical representation of assumptions used to derive the Quasi-Isotropic Beam Steering Algorithm.

As done with beam steering, the array of sensors is manipulated to act as a single transducer by combining the sensor spacing and the arrival times. For N sensors in the array, the slope of the two variables plotted against each other can be multiplied by the propagating wave velocity to determine θ. Figure 18 shows a normalized plot of the arrival times as a function of sensor spacing for an array of four sensors and the resulting slope. The solution is then found by solving for θ:

$$\theta = \cos^{-1}[bv] \qquad [32]$$

where:

$$b = \lim_{\alpha \to 0} \frac{\Delta t}{\Delta \alpha} = \frac{dt}{d\alpha}$$

4.2.2 Anisotropic Case

For accurate locating in anisotropic materials, it is important to consider the variations in the material properties. Lamb wave velocities are orientation-dependent due to the anisotropy of the elastic properties. From the quasi-isotropic lay-up configurations used in the polymer-based composites under investigation, it was found that the velocity profiles can be fit to a trigonometric function that take into account the material anisotropy for most material layups (see Section 3.3.3).

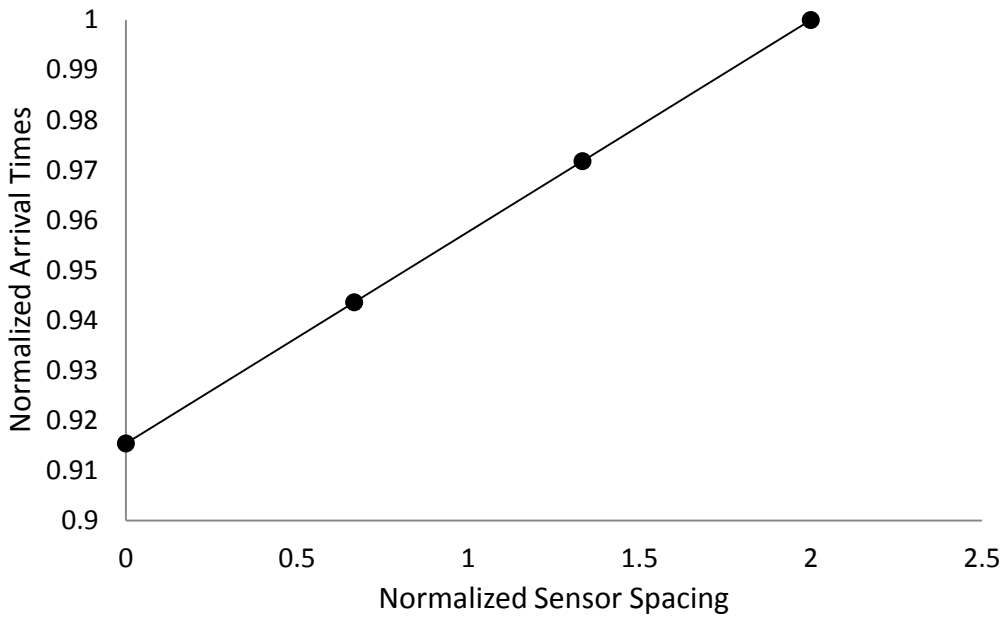

Figure 18. Plot showing how the arrival times and sensor spacing are manipulated to act as a single transducer for a linear array of four sensors and the resulting slope.

Using simple assumptions from beam steering and quasi-isotropic material systems, a quasi-isotropic beam steering algorithm for anisotropic materials is derived. In the isotropic case, it was assumed that the wave travels at the same rate in all directions; this is not the case for anisotropic materials, as was seen in Figure 7. For the assumptions made in the isotropic case to hold, the definition of δ needs to be modified. The modification can be made by simply acknowledging that velocity is a function of orientation as well as frequency as follows:

$$\delta = \mathrm{C}_f(\theta) * \Delta \mathrm{T}_{i,i+1} \qquad [33]$$

where $C_f(\theta)$ is given in Equation 15. This modification only holds assuming the sensor spacing α is small compared to the distances from the arrays to the impact location. If the distance from the impact to the array approaches that of the sensor spacing, the difference in angle from each sensor to the source will become large enough that the wave speeds will result in a nonlinear timing sequence. As a consequence, the method will also fail if the impact occurs at 90^0 from the center of the array.

An equation can be found relating the sensor spacing, α, arrival time shift parameter, δ, and the phase velocity to find the angle at which the impact intersects the arrays. Equation 31 is modified to include material anisotropy by incorporating the anisotropic wave velocity as follows:

$$\cos\theta = \frac{\delta}{\alpha} = \frac{C_f(\theta) * \Delta T}{\alpha} \quad [34]$$

The velocity equation as a function of orientation was given in Equation 15 and transformed with a phased shift of π to the following equation:

$$C_f(\theta) = A\cos(2\theta + \pi) + B \quad [35]$$

where A and B are fit parameters relating to amplitude and vertical shift, respectively. Plugging this into Equation 34 and solving for theta, the following beam steering equation is found using trigonometric identities and basic algebra:

$$\theta = \cos^{-1}\left[\frac{-\frac{\alpha}{\Delta T} \pm \sqrt{\frac{\alpha}{\Delta T}+8A^2+8AB}}{4A}\right] \quad [36]$$

Using Equation 36 for each array, where α/ΔT is found from the slope of the two variables plotted against each other (see Figure 18), a ray is generated that extends from the array center in the estimated direction of the source. The estimated location of the impact site is then found by calculating the intersection of the rays from a minimum of two arrays, as seen in Figure 15.

4.2.3 Theoretical Error Analysis

Theoretical errors are found by using the experimentally determined velocity profile presented in Section 3.3.3 for the stiffness critical structure. By exciting the medium with a stationary transducer, a phase point can be tracked for a given length of time and distance and the resulting velocity found as a function of orientation, as seen in Figure 8. Using a theoretical grid of impacts locations, the velocity profile is used to calculate the arrival times and the location algorithm used to calculate the estimated theoretical distance to the source. The error between the estimated theoretical location and the actual theoretical location is then found and used to generate a three-dimensional error plot.

Each Intersection on the grid is considered as an impact location. A mesh size of 1” in both the x and y direction is used for calculating the theoretical errors. At each impact location, the velocity profile is used to calculate the time of flight from the

source to each sensor. The calculated time of flight is then used as the arrival time input for the location algorithm. The estimated location of the source is then calculated and the error between the location of the actual source and the estimated source is then found using the following equation:

$$r = \sqrt{(x_{actual} - x_{calculated})^2 + (y_{actual} - y_{calculated})^2} \quad [37]$$

The theoretical error found at each impact location is then arranged in a three-dimensional plot where the x and y axes are the coordinates of the impact locations and the z-axis is the error between the actual location and the theoretically determined location. This allows inaccuracies in the location algorithm to be seen visually and any trends present in the algorithms to be identified for establishing the optimal array placements on each component.

Figure 19 shows the resulting theoretical error plot found from analysis performed on the quasi-isotropic beam steering algorithm using the velocity profile found for the stiffness critical structure. As seen in Figure 19, the errors are high, indicating an error in the assumptions used to derive the location algorithm. The error can also be seen by comparing the estimated angle of the source from each array to the actual angle (see Figure 20). Theoretically, the estimated angle versus the actual angle should have a one-to-one relationship. As seen in the plot, however, the estimated angle is typically 25% off from the actual angle. The source of the error can be identified

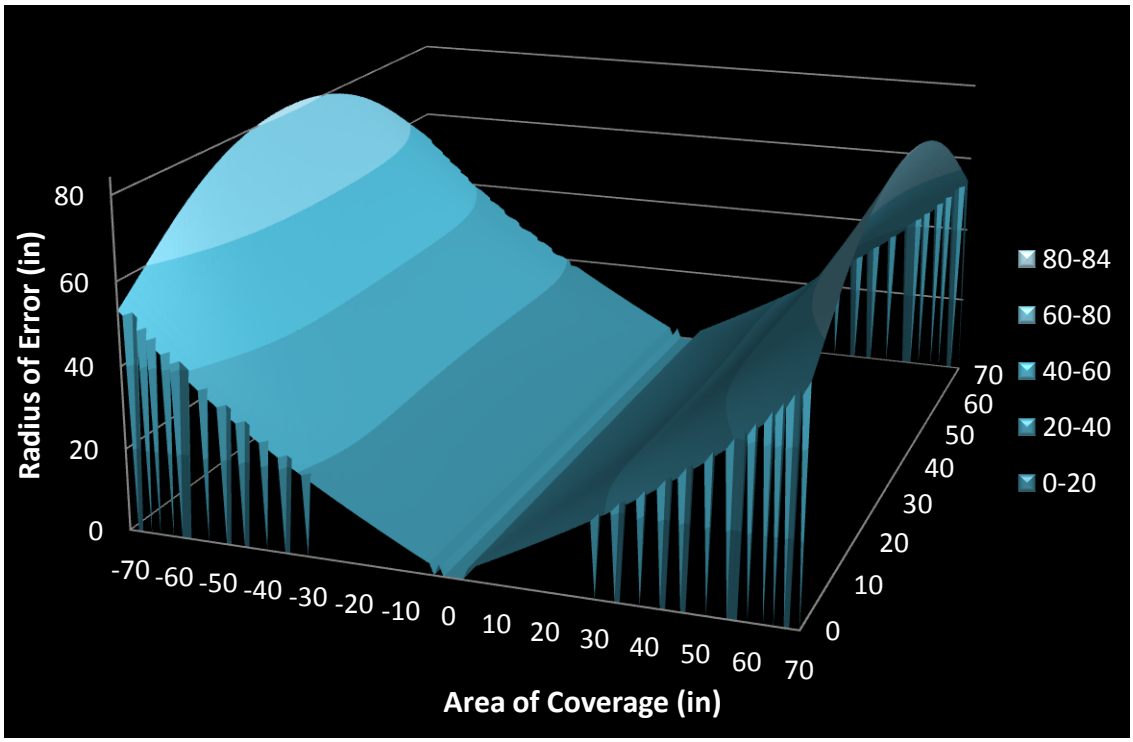

Figure 19. Theoretical error plot for the quasi-isotropic method.

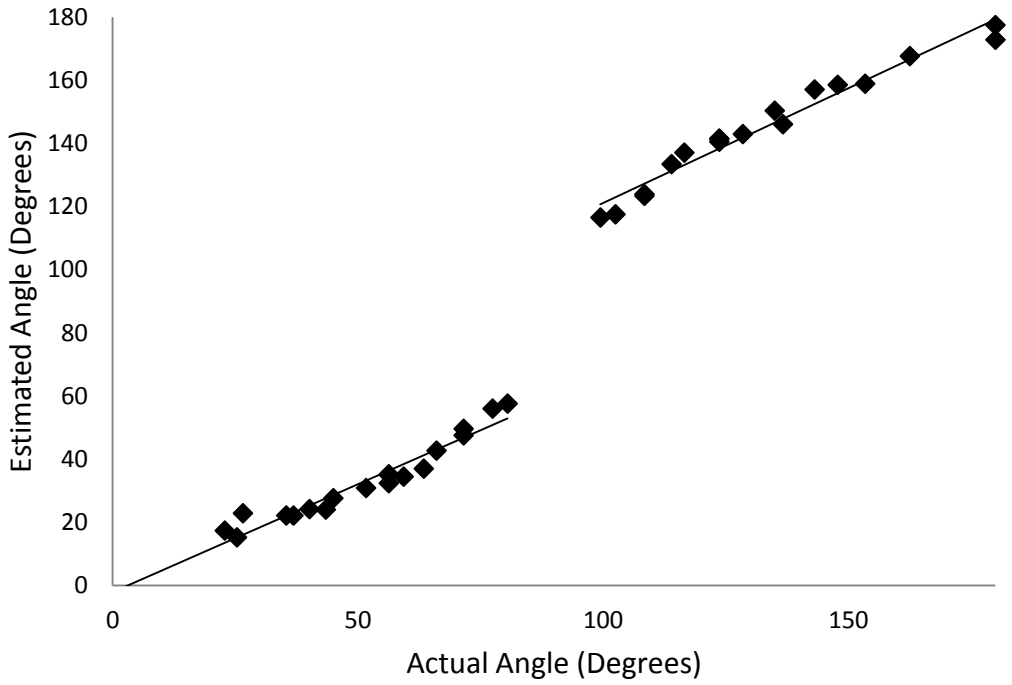

Figure 20. Estimated angle using the quasi-isotopic method compared to the actual angle.

upon closer inspection of the phased array delay laws concerning beam steering.

As was seen in Equation 27 and Figure 13, beam steering utilizes a linear relationship between the timing sequences from sensor to sensor in the array. This assumption was used to derive the quasi-isotropic beam steering method by assuming that the angle between each sensor in the array to the source was approximately equal. This assumption, as it turns out, is incorrect since the arrival times are in fact dependent on each individual sensor's location in space relative to the source. This implies that the algorithm is combining beam steering with beam focusing where beam steering was used to derive the equations; however, the arrival times incorporate beam focusing. When using beam steering, the source of the event must be assumed as a line source such that the angle from each sensor to the source is exactly the same, as seen in Figure 21. As a consequence, the initial assumptions result in a difference in arrival time from sensor to sensor that is nonlinear.

To verify the new assumption of a line source, a relationship had to be determined translating a point source to a line source. This relationship can be seen by combining Figure 21 with Figure 17 and is shown graphically in Figure 22. In order to steer the beam in the given direction of the impact, the angle from each sensor to the source must be exactly the same. The line source must then be parallel to the resulting linear wave front. As seen in the graphical representation shown in Figure 22, the shift in arrival time from each sensor must be equal to multiples of the time shift parameter δ. The procedure used to verify the new assumption is as follows:

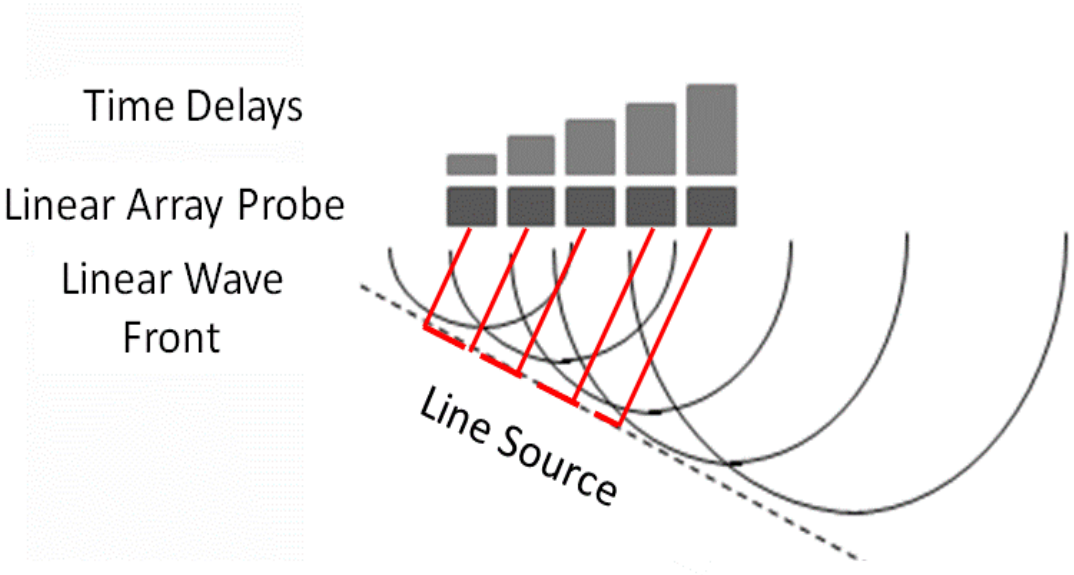

Figure 21. Schematic showing the correct assumption for beam steering of a line source as opposed to a discrete location used in beam focusing.

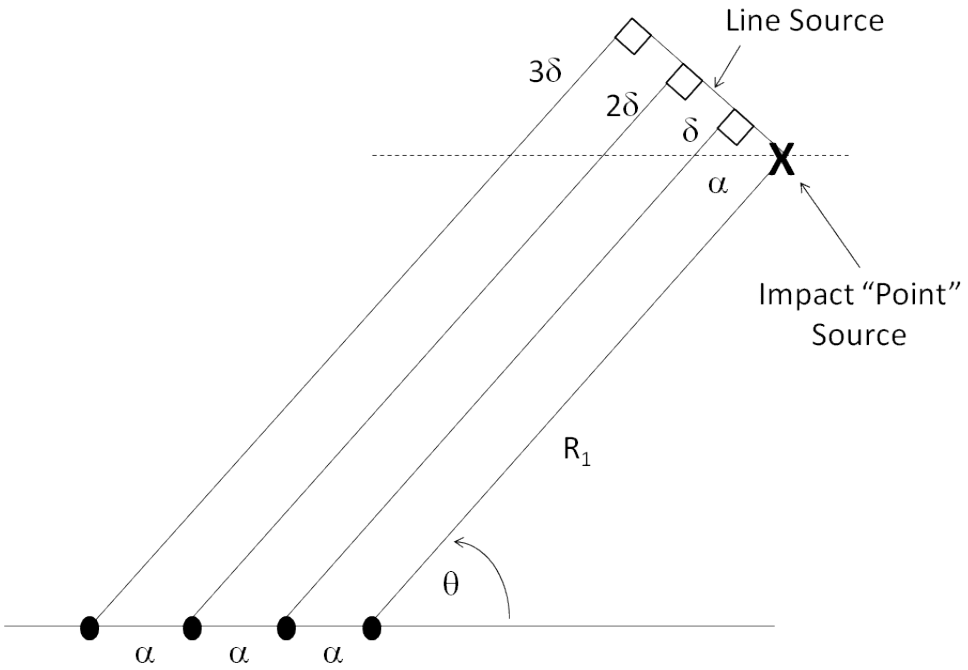

Figure 22. Schematic describing the actual time shift needed to produce beam steering in the quasi-isotropic beam steering algorithm.

1) Find the time of flight (TOF_n) from each sensor to the impact point using the velocity profile given in Equation 15.
2) For each array, determine the actual angle to the source, θ_i.
3) Find the velocity of the wave in the given direction for each array, $C(\theta_i)$, using Equation 15.
4) Determine the time shift parameter using Equation 34 ($\delta = v_f \Delta t$) for each array:

$$\Delta t_i = \frac{\alpha \cos(\theta_i)}{C(\theta_i)} \quad [38]$$

5) Find the new arrival times with applied time shift:

$$t_n = TOF_n + (n-1)\Delta t_i \quad [39]$$

where n = 1 is the first arrival sensor in the array.

6) Using the location algorithm, determine the estimated source.
7) Find the error using Equation 37.
8) Repeat for all impact locations

Figure 23 shows the resulting three-dimensional error plot for the quasi-isotropic beam steering algorithm with the applied time shift. As seen in the plot, the assumption that the source must be considered a line source is correct as the errors are very small,

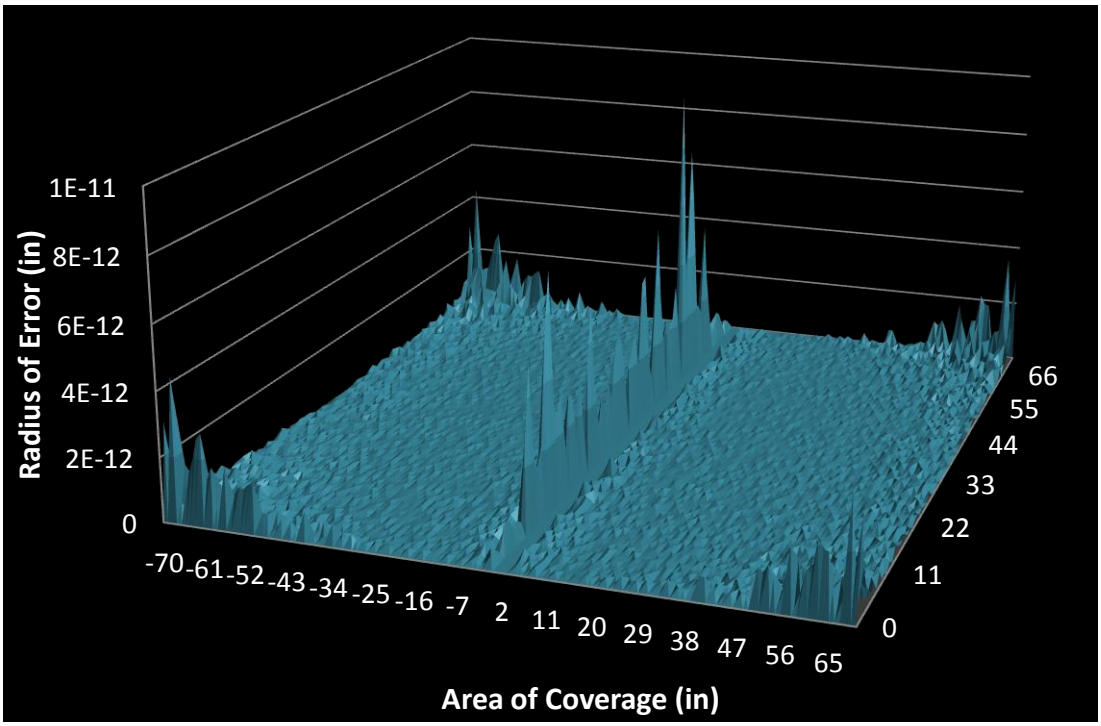

Figure 23. Theoretical error plot for the quasi-isotropic algorithm with applied time shift.

approximately zero, for all locations on the grid. This assumption indicates velocity in anisotropic mediums is strongly orientation-dependent even for small sensor spacing's and large distances from the arrays to the impact locations. Note also that the errors spike up in the regions parallel and perpendicular to the arrays. The spike in the errors from events located perpendicular to the arrays are due to the arrival times becoming nonlinear and as such, beam focusing techniques should be employed. For events parallel to the arrays, the inaccuracy is attributed to the geometry of the arrays and the sensor spacing. The reader is referred to references (17) and (18) for more on this phenomenon.

By looking at the source to sensor, a global velocity profile was found and fit to a

beam steering equation; the quasi-isotropic method. The quasi-isotropic method was derived using assumptions taken from beam steering techniques; however, the arrival time from sensor to sensor still contained elements of beam focusing. Another future source of error is identified by considering the complex interactions of plate waves with the geometrical changes associated with the design and shape of the composite material as well as other parameters such as material degradation and manufacturing concerns. If local material degradation, geometrical changes, or manufacturing flaws are imbedded in a large composite structure, the global velocity profile will break down, resulting in inaccurate source location. To mitigate these issues, a new method was derived where the sensor-to-source approach is utilized instead of the source-to-sensor approach used in the quasi-isotropic beam steering equation.

4.3 Vector Velocity Method

The vector velocity method is developed empirically from data collected per component. This increases the accuracy in locating by tailoring each location algorithm directly to the component being tested. As was seen in both the quasi-isotropic and triangulation techniques for location determination, the source-to-sensor approach introduces errors by assuming that the global velocity profile remains constant at all locations on a given structure. From experimental tests, it was found that the velocity profile can change due to:

- Component size
- Geometry

    - Shape
    - Holes/cutouts
    - Thickness changes
    - Joints/bonds
    - Design
- Material changes
    - Honeycomb core
    - Liners
    - Solid laminate
    - Joints/bonds
    - Thickness changes
- Manufacturing
    - Process control
    - Operator error
- Defects/flaws
    - Planned
    - Unplanned

For these reasons, the following method was developed to locate the source of an event based on beam steering phased array techniques and experimental data collected per component using the sensor-to-source approach.

The quasi-isotropic beam steering location algorithm showed a strong dependence of velocity on angular position in anisotropic materials. To this point,

analysis has been based on the source-to-sensor approach. Upon applying this method to complex structures with multiple cut outs, geometrical changes, ply build ups or drops, complex layups, liners, induced damage zones, material degradation, and manufacturing variability, the global velocity profile was found to become warped and very complicated. Due to the complex interactions of plate waves with the conditions listed, a new method based on the sensor-to-source is developed in the following paragraphs in an attempt to increase accuracy. Using this approach, the local velocity profile at the location of each array is used, allowing the variables affecting the global velocity profile to be neglected.

Using the reverse method, sensor-to-source, the local velocity profile near each array's position is determined and fit to an equation. This method reduces the errors in locating by looking only at the local velocities near the arrays, thereby incorporating any effects that the geometry, material degradation, and manufacturing concerns may have on the global wave speeds. By looking at the velocity as a vector, the linear arrays themselves can be used to measure the local horizontal component of the velocity vector (see Figure 24) by the slope of the sensor positions to the arrival times as was done in the quasi-isotropic method. Using this method, a series of elastic impacts are performed on the component in the area of desired coverage at a number of predetermined locations in a manner similar to that done for finding the theoretical errors, as presented in Section 4.2.3. Using these data, the arrival times are found and used to determine the resulting local horizontal velocity component for each impact location and plot versus the incident angle from the sensors to the source. Each array is

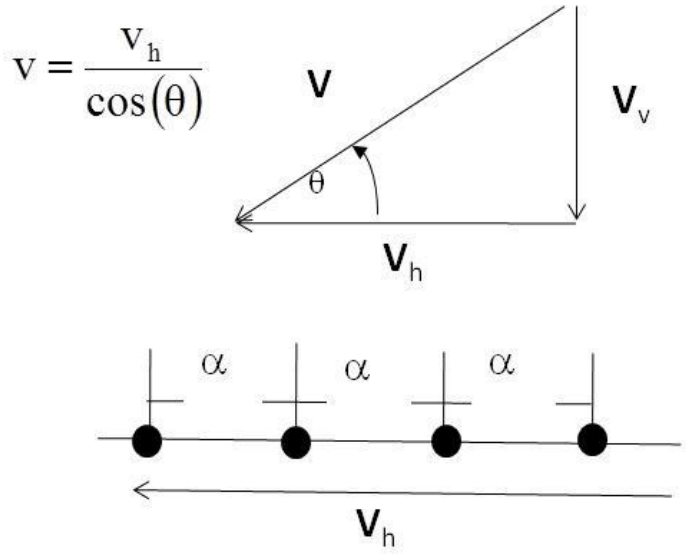

Figure 24. Schematic indicating how a single linear array can be used to determine the local horizontal component of the phase velocity.

then split into two zones and each zone is then fit to an equation used to steer a beam from both arrays that intersect at the estimated location (see Figure 25). Each array is split into two zones due to the following:

- The local horizontal velocity will be either positive or negative depending on the direction of the incoming phase front.
- Due to the many variables affecting the velocity profile, it is assumed that the determined local velocity profile will not be symmetric in that more accurate approximations of the profile can be made by splitting the arrays into zones.

The method is demonstrated in the following few paragraphs.

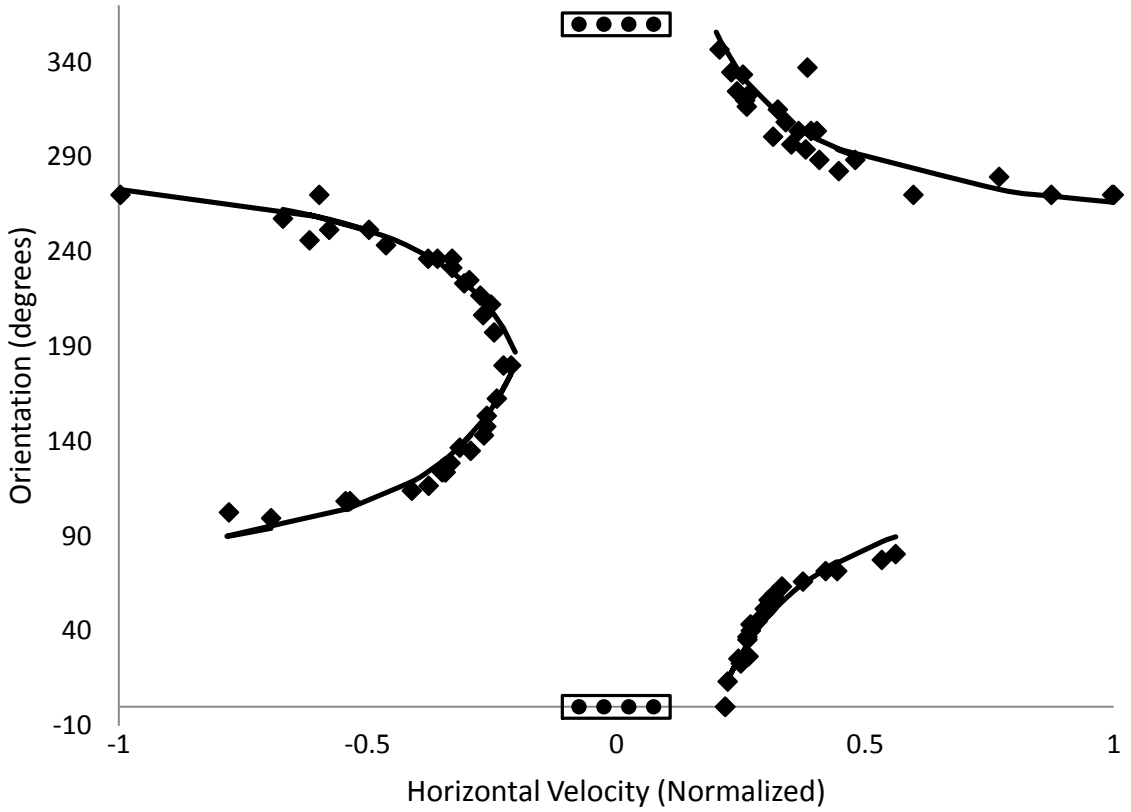

Figure 25. Local horizontal velocity profile found using the vector velocity method for the stiffness critical structure.

Each array is placed on the component and the sensor position per array recorded in terms of the components boundaries. For this work, two linear arrays were used so as to minimize the sensor density and while maximizing the area of coverage. Next, a grid is made on the component being tested and elastic impacts performed at each intersection on the grid. The spacing of the impacts is such that a wide range of angles from the horizontal of each array to impact source are obtained. The local horizontal velocity is then computed from the slope of the sensor positions versus the arrival times, resulting in the following equation (see Figure 24):

$$V_h = \lim_{\Delta t \to 0} \frac{\Delta \alpha}{\Delta t} = \frac{d\alpha}{dt} \quad [40]$$

By plotting the orientation of the source with respect to the local horizontal velocity, a relationship can be seen in Figure 25 relating the two values. As seen in the plot, the orientation of the source is inversely proportional to the local horizontal velocity. It can also be seen that the assumption of nonsymmetric local velocity profiles due to material anisotropy, geometrical features, material degradation, and manufacturing variability was correct. It should also be noted that if the arrays were split further into more zones, the fit to the local velocity profile will likely become more accurate. By fitting two parameters, A and B, an empirical equation is found relating orientation to the measured local horizontal velocity:

$$\theta(V_h) = \frac{A}{V_h} + B \quad [41]$$

Upon inspection of Equation 41, it can be seen, after plugging in Equation 40, that the equation takes a similar form as the beam steering time delay law presented in Equation 27.

4.3.1 Theoretical Error Analysis

Using the same method for theoretical error determination as was presented in Section 4.2.3, it can be seen in Figure 26 that the errors are much less than those using

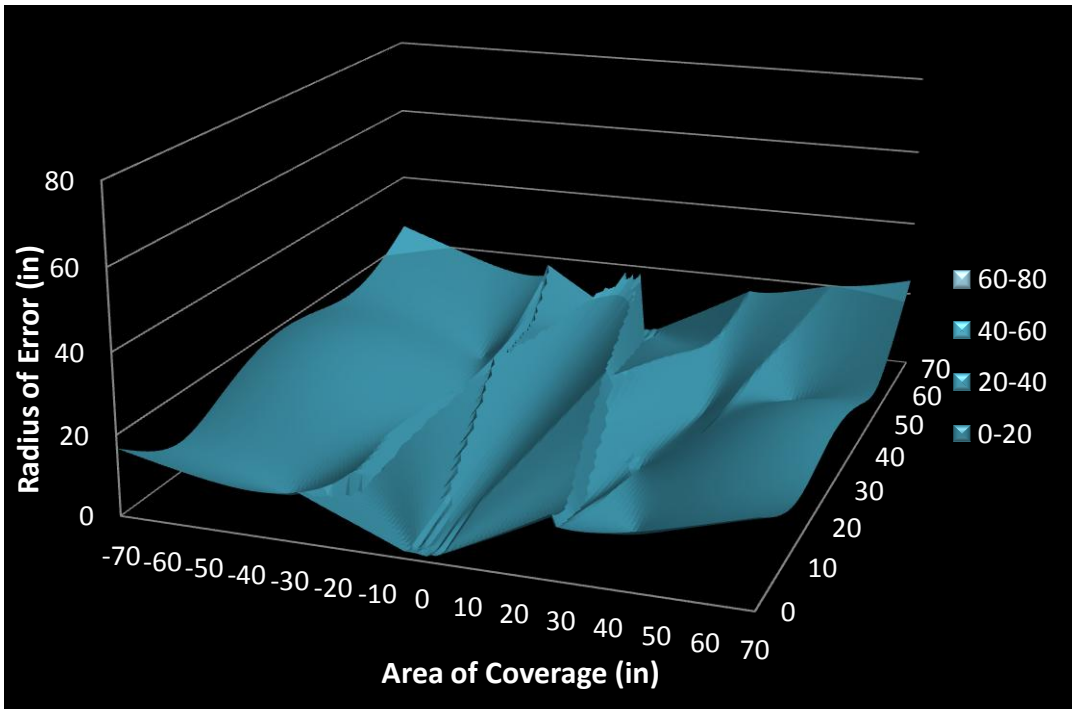

Figure 26. Theoretical error plot for the vector velocity method.

the quasi-isotropic method. Here, the errors result from the fact that the algorithm itself was derived using the empirically determined local velocity profile where the arrival times were determined theoretically based on the experimentally determined global velocity profile. As seen in Figure 27, the estimated incident angle to the actual angle is of high accuracy, approximately a one-to-one relationship as would be expected. This method proves to be the most versatile location algorithm due to its ability to take into account manufacturing variability, anisotropy, material degradation, and other factors that can affect the local versus global properties of the structure.

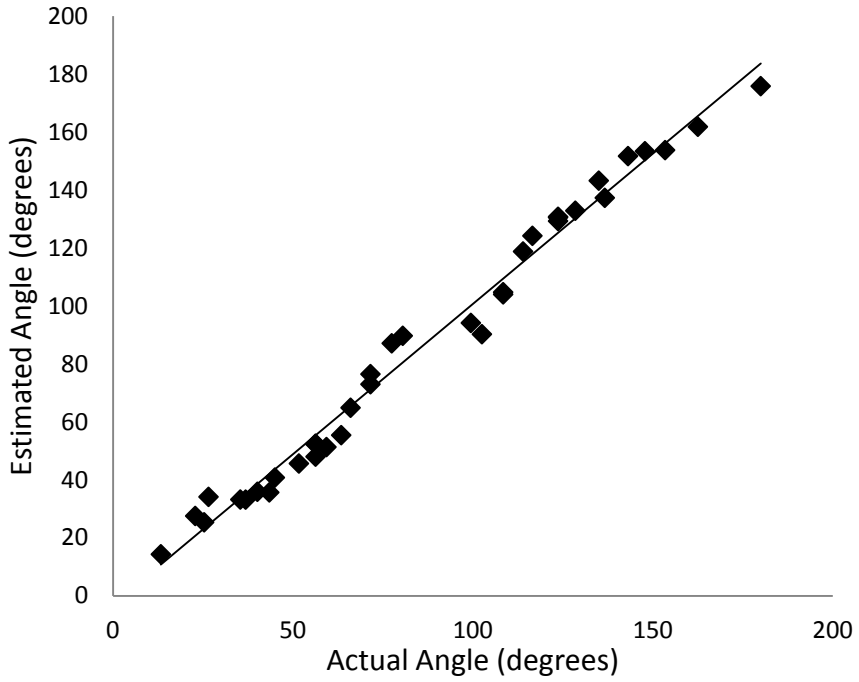

Figure 27. Estimated orientation using the vector velocity method vs. actual angle as performed on the stiffness critical structure.

4.4 AIMS Beam Steering Location Software Algorithm

To support automation of the impact detection system, the beam-steering concept was integrated into a LabVIEW-based software application called AIMS (Automated Impact Monitoring System) Beamforming by Digital Wave Corporation. This algorithm was developed by Digital Wave Corporation during this study and was evaluated as part of this work. The AIMS beam steering formula was derived using the same process used for the quasi-isotropic method except the axes are rotated by 90 degrees such that the vertical axis is now the zero degree axis, resulting in the use of sine instead of cosine in Equation 34:

$$\sin(\theta) = \frac{v * \Delta T}{\alpha} \qquad [42]$$

The velocity profile is determined empirically in a manner similar to that of the vector velocity method using the sensor-to-source approach so as to reduce error due to local-to-global material changes. A series of elastic impacts are performed on the structure and the velocity solved for using the beam steering formula given in Equation 42 where the angle from the source, sensor spacing, and the arrival time information are known. The velocity profile is compiled for each array and each profile is fit with a fourth-degree polynomial to account for material anisotropy and local-to-global material changes. Figure 28 shows a velocity profile fit for one array on the stiffness critical structure where the white squares are the calculated velocities from the known impact locations.

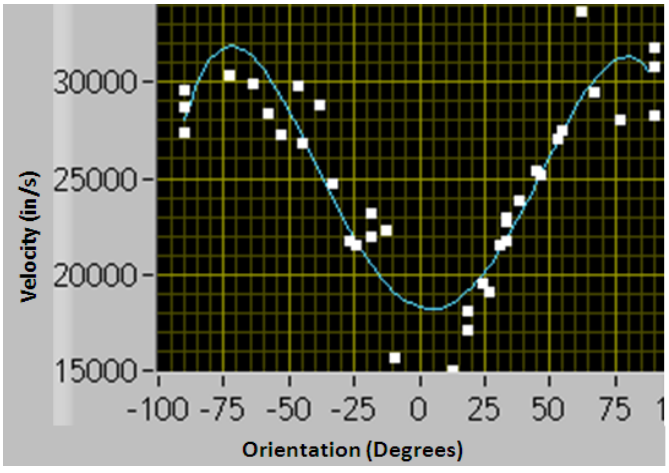

Figure 28. Fit velocity profile for a single array to the impact data using the AIMS software algorithm.

A semi-automated arrival time determination feature was incorporated into the software to help identify the correct phase points that are used to determine the velocity profile and for locating the source of events (Figure 29). This feature allows the phase points on the first two sensors per array to be selected manually then, using a "snapping" algorithm, the phase points on the remaining sensors are snapped into position. The "snapping" algorithm linearly extrapolates the location of the phase points on the remaining sensors using information gathered from manual placement of the first two points.

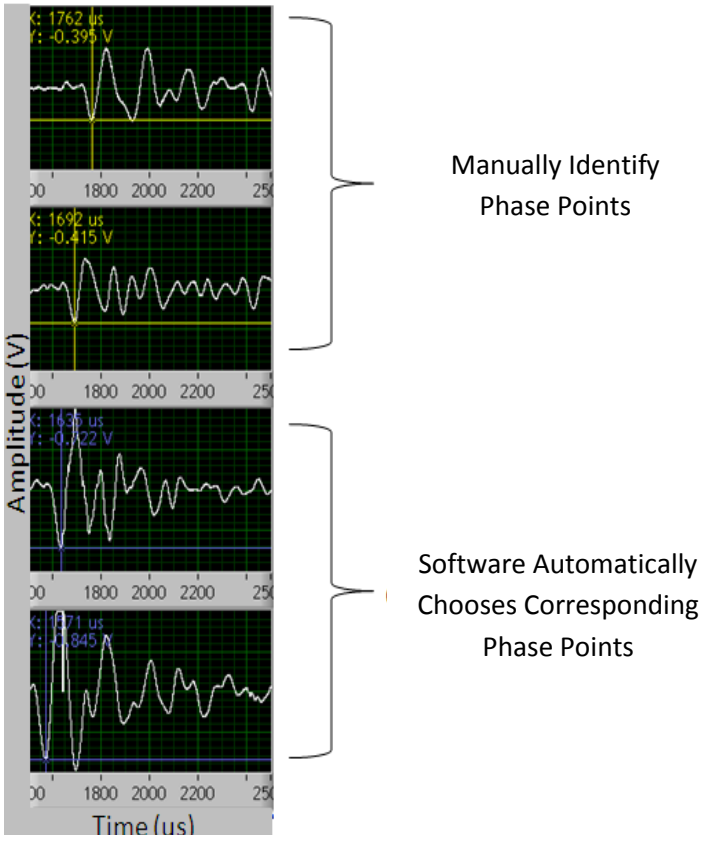

Figure 29. Plot showing how the automated arrival time software works (AIMS Beamforming software).

The location algorithm uses the same method to locate events as the previous algorithms by determining the intersection of the beams steered from both arrays (as was shown in Figure 15). This method is completely automated except for determination of the phase points. Error bars in the estimated location are incorporated by determining the standard deviation in the difference between the actual velocities determined experimentally and the velocity fit equation. This standard deviation is then added and subtracted to the velocity used to determine the estimated angle to the source providing an area of probable occurrence. Figure 30 shows a diagram indicating the location of the two arrays and the estimated source location with error bars. The impact location is at the intersection of the two center lines where the two rays surrounding them are error bars. The horizontal line is a one-dimensional triangulation estimate to aid the software in locating the correct intersection of the two arrays.

4.4.1 Theoretical Error Analysis

Figure 31 shows the resulting theoretical errors using the AIMS Beam Steering algorithm. The theoretical errors were found using the same approach laid out in Section 4.2.3. Note that the errors are not zero since the phase velocity profiles used to determine the arrival times was a global velocity profile where the calibration velocity profile was experimentally determined locally at each array. The errors are slightly larger than seen in the vector velocity method; however, the results are symmetric for each zone.

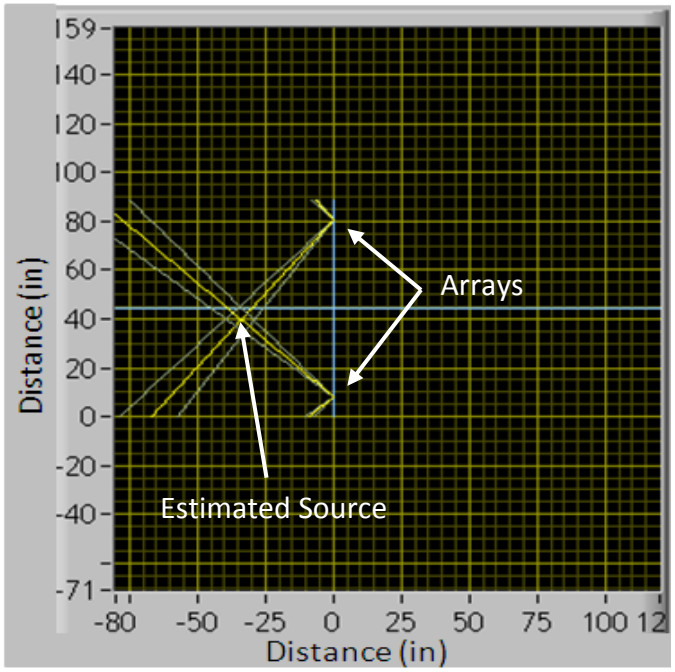

Figure 30. Estimated source location found from two rays extending from each array found from the AIMS Beamforming algorithm.

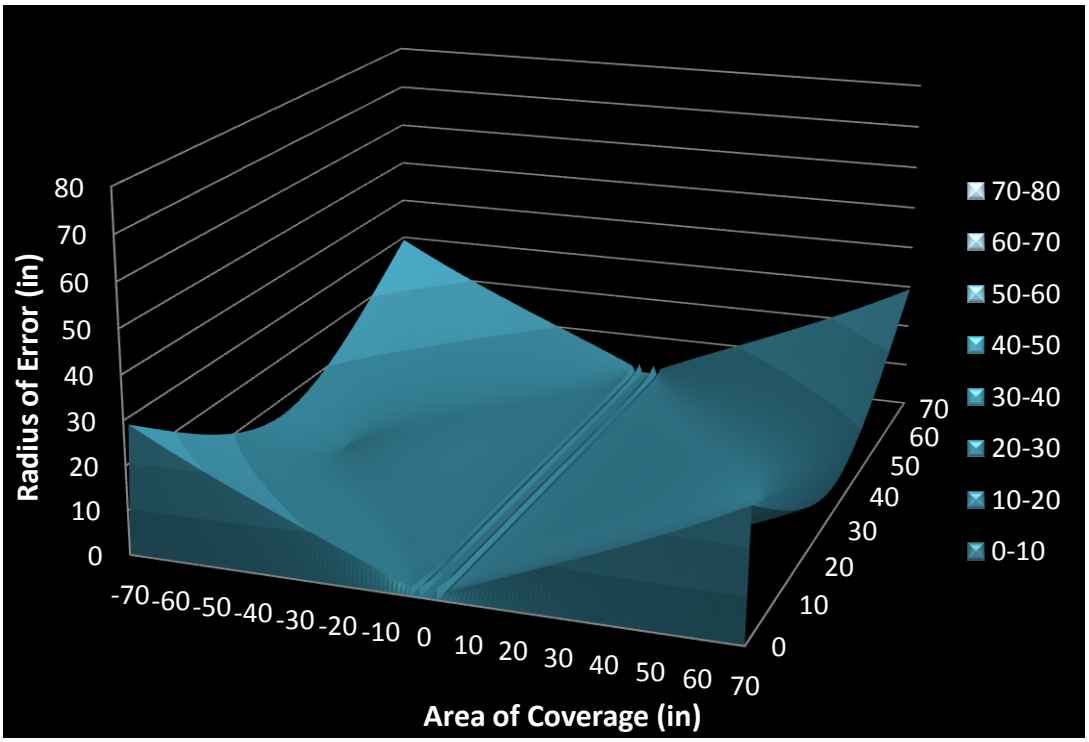

Figure 31. Theoretical error plot for the AIMS beam steering algorithm.

Table 1 indicates that both the vector velocity and AIMS location methods have average errors in the range required to satisfy the demands of this work. The quasi-isotropic method was shown to be too inaccurate and incorporation of the time shift method much too complicated and not likely to work well in actual applications as the other two methods will. Also note that the theoretical error plot found for the velocity vector method in Figure 26 is not symmetric, as is the case for the other two methods. The reason for this is seen in the derivation of the velocity vector algorithm. The algorithm was derived by splitting the area of coverage into two zones for each array, leaving four zones each with its own velocity fit equation for calculating the angle to the source. This means that each zone will result in slightly different values then the others, resulting in a nonsymmetric error plot.

Both the velocity vector method and the AIMS beam steering algorithm show promise for location estimation in real applications. Both methods are derived based on the sensor-to-source approach, simplifying the complexities involved with material anisotropy, manufacturing concerns, material degradation, local-to-global material changes, and geometrical changes. The AIMS method appears to be smoother in that it

Table 1. Theoretically determined average, minimum, and maximum errors for the three beam steering algorithms.

	Average (in)	Minimum (in)	Maximum (in)
Quasi-Isotropic Algorithm	31.40	2.72	81.43
Velocity Vector Algorithm	9.27	0.13	25.14
AIMS Algorithm	5.49	0.01	29.46

is constant (symmetric) in its results; however, the vector velocity method appears to be more accurate further from the arrays. Also note that the AIMS beam steering algorithm has already been developed into a software package where the velocity vector method has not.

Beam steering techniques have the advantage of being able to locate at large distances from the arrays. The disadvantage of the beam steering technique is that two arrays are required to locate the source. In actual components that contain complex geometries (e.g., cutouts, ply-buildups, features), it is not always possible to ensure that the entire component can be covered with two arrays at all locations. Where beam steering cannot be used, another location technique based on beam focusing can be utilized as well as the Tobias triangulation method. The beam focusing technique only requires a single array and can be implemented in areas where wave propagation line-of-sight can be limited.

4.5 Beam Focusing Algorithm

All previous location algorithms have been focused on beam steering. As a means of further reducing the number of sensors required for source location, the beam focusing technique is now explored. The beam focusing location only requires a single array of sensors with a minimum of three sensors for source location. As will be shown, a system of equations are found and solved for where each equation utilizes two sensors to solve for a hyperbola. When a minimum of two hyperbolas are combined

from three sensors, the point of intersection is the point of estimated impact (see Figure 32 and Figure 33).

The derivation for the beam focusing algorithm is derived here for a linear array of N sensors. Considering only the isotropic case, it is assumed that the wave front will travel from the impact sight with a constant radius in all directions. The distance the wave propagates from the impact to each sensor can then be assumed to be equal to R_i. Drawing a circle of radius R_i centered on each sensor in the array, it is seen that the impact location occurs at the location of the intersection (see Figure 34). A relation can then be found relating each radius of sensor to impact distance for an array of N sensors as follows (equation of a circle):

$$\mathrm{R_i^2} = (\mathrm{x} - \mathrm{h}_i)^2 + (\mathrm{y} - \mathrm{k}_i)^2 \text{ where } i = 1, 2, 3, \ldots \mathrm{N} \quad [43]$$

where (h_i,k_i) are the x and y coordinates, respectively, for the location of each sensor. Applying this concept to all sensors used in the array, a relation is obtained relating the difference in radius from two sensors to the difference in arrival times of two sensors as follows:

$$\left|\mathrm{R}_i - \mathrm{R}_j\right| = \delta_{ij} \text{ where } i \neq j \quad [44]$$

$$\delta_{ij} = \mathrm{V} * \Delta\mathrm{T}_{ij} \quad [45]$$

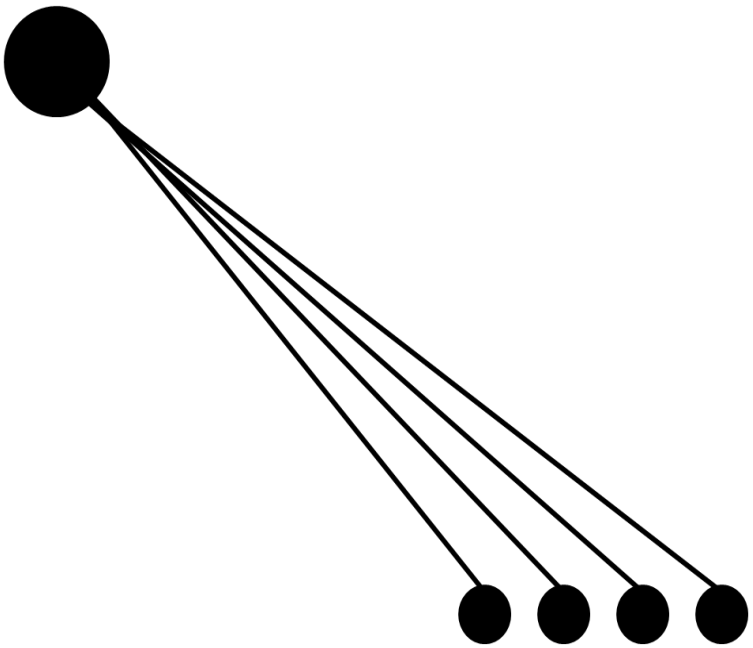

Figure 32. Schematic diagram of beam focusing.

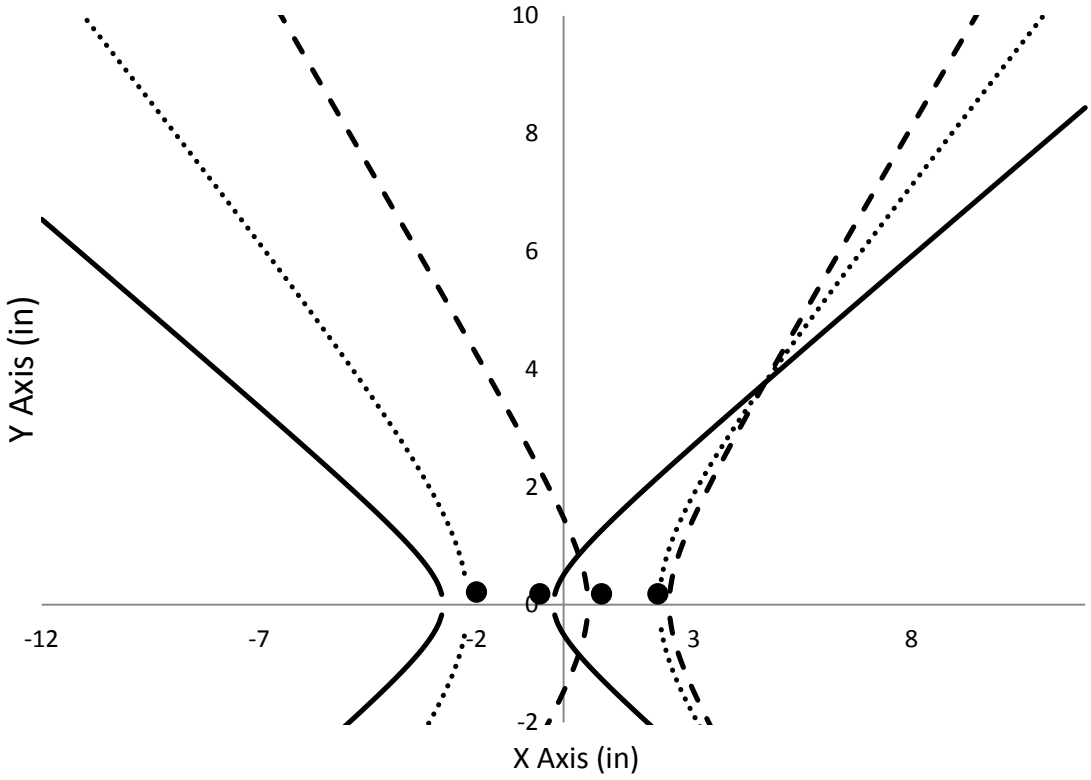

Figure 33. The intersections of hyperbolas found for a given pair of sensors intersects on the location of estimated impact for a linear array of four sensors.

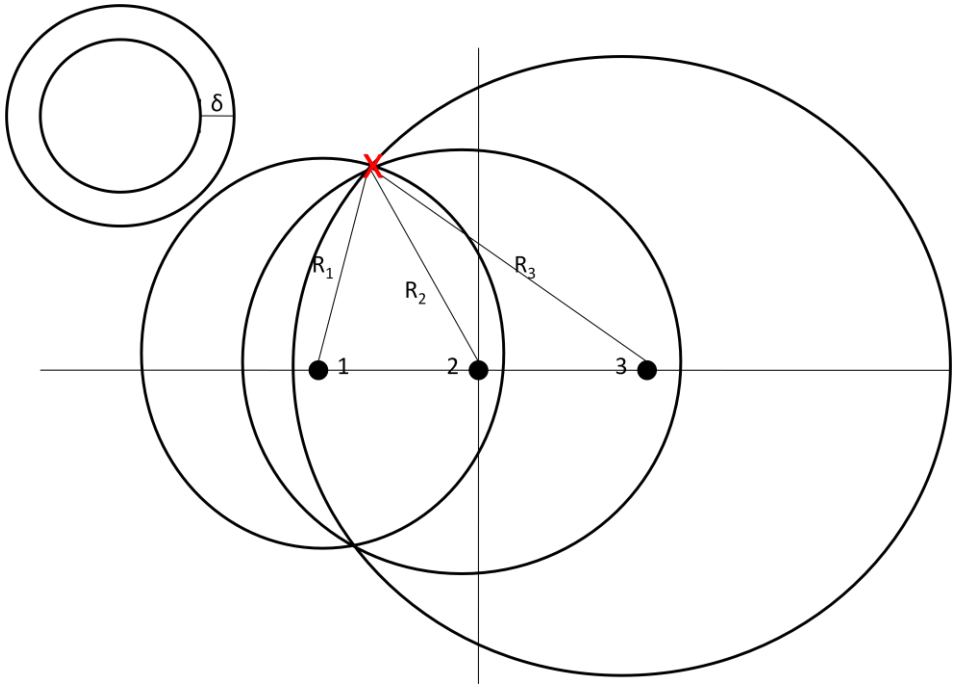

Figure 34. Radius of possible impact locations for each sensor and the relationship to velocity and change in time necessary to derive the beam focusing equation.

Substituting Equation 43 and 45 into Equation 44 and solving for y in terms of x, a system of hyperbolas are found that can be used to estimate the point of intersection and therefore the estimated point of impact (as seen in Figure 32 and Figure 33).

The disadvantage is that the beam focusing accuracy in estimating impact location is highly dependent on the distance between the impact and array. The confidence envelopes for estimated impact location becomes an elongated ellipse where the major axis is directly related to the distance from the detecting array (see Figure 35). It was concluded that beam focusing should not be utilized to cover large regions due to the decreased confidence with increasing distance. Also, for the case of anisotropic material systems, the wave speed as a function of orientation causes the derivation to become impossible to solve for with three unknowns and only two

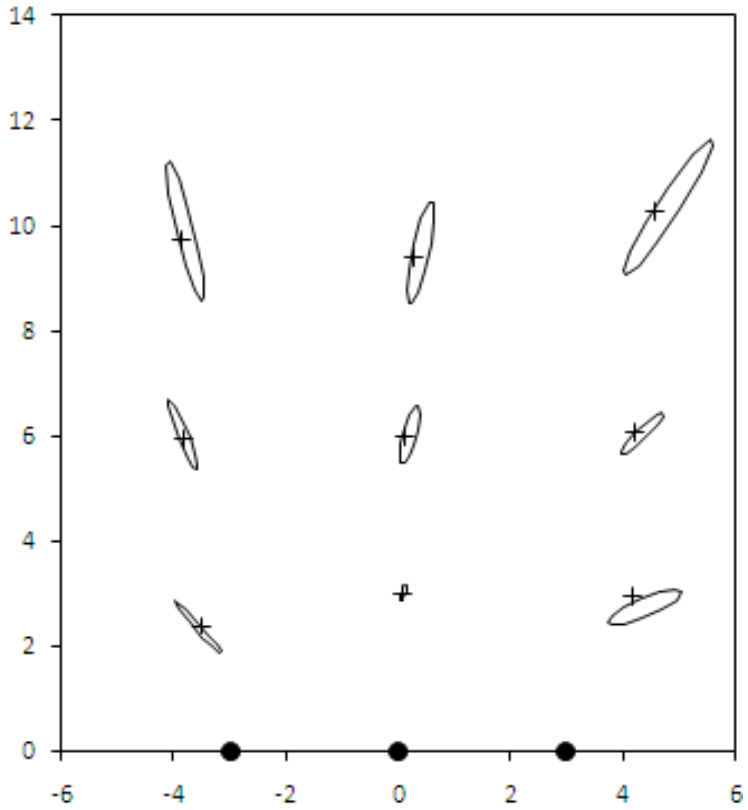

Figure 35. Map of trial impacts on an aluminum specimen showing the impact locations (+), MAE sensors (circles), and computed 95% confidence envelope computed using the beam forming phased array technique.

equations. However, using one array, the beam steering algorithm can be used to determine the estimated angle to the source, plugged into the velocity profile equation, and the correct velocity calculated and used in the beam focusing algorithm.

Utilizing the advantages of phased array techniques, it is possible to optimize the array positions to maximize the accuracy of the impact location estimates while minimizing the number of sensors and the amount of cabling required. While the optimization of the array placements is still ongoing, it is estimated that coverage over an area of approximately 240 ft^2 with complex geometries can be achieved using

between 12-16 sensors (3-4 arrays) and less than 100 feet of cables. Using traditional triangulation techniques, similar coverage would require 24 sensors and approximately 200 feet of cabling to achieve the same accuracy in locating events. As the beam steering and focusing algorithms and hardware become more accurate and advanced, the number of sensors and required cabling will be reduced even further, resulting in a robust, low profile, low sensor density impact detection system capable of monitoring the health of structures in real time.

CHAPTER 5

INSTRUMENTATION

Two different data acquisition systems were used to perform impact detection and characterization tests. The first is a lab system used to characterize the material system under investigation while the second is a compact portable data acquisition system. Both systems were manufactured by Digital Wave Corporation[3] where the portable system was developed in conjunction with ATK. The following sections identify the key components of each system and the types of sensors under investigation for optimal impact detection performance.

5.1 Lab Data Acquisition System

The lab system is used to characterize the material system under investigation to optimize event location. This system consists of a computer, data acquisition system, signal conditioning, preamplifiers, piezoelectric sensors, and cables (see Figure 36).

When an event occurs, an elastic wave is initiated and propagates to the sensors where the sensors convert the mechanical wave into an electrical signal that is then

[3] Digital Wave Corporation, 1370 E Arapahoe Road, Centennial, CO USA 80112; 303-790-7559

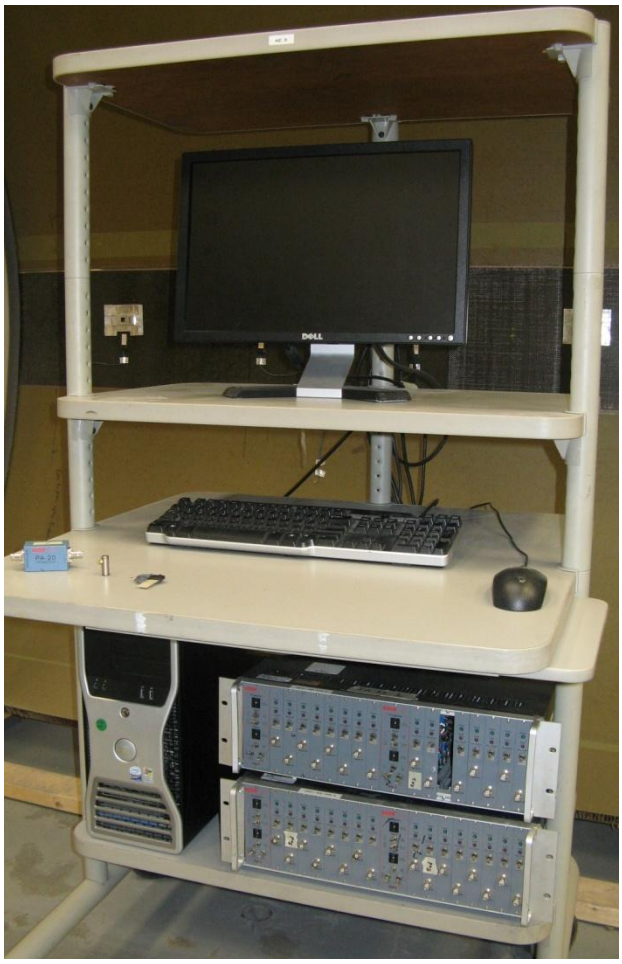

Figure 36. Lab system developed by Digital Wave Corporation.

amplified by preamplifiers to the signal conditioning board (FM1). The FM1 conditions the signal by filtering out unwanted frequencies, setting trigger levels to increase or decrease sensor sensitivity to events, and then amplifying the signal to the data acquisition board in the analysis computer. Digital Waves WaveExplorer software is then used to analyze and displace the waveforms.

The signal conditioning board (FM1) operates at 20 MHz with a 16 bit processor and can be configured to handle a range of 4-96 sensors at any given time. The FM1 has a wide range of filtering and amplification capabilities, making it a very versatile tool for

interrogation of materials both in the lab and in the field (see Table 2). The FM1 operates at a band width of 20 kHz to 5 MHz and utilizes nondistorting linear phase Bessel filters. The FM1 also generates power output for each channel to power preamplifiers, reducing the need for extra cables.

WaveExplorer is an analysis package that allows the user to set the sampling rate, number of points in the waveform window, pretrigger points in the waveform window, voltage range, and parametric sampling rate prior to testing. Defining these parameters prior to testing increases the ability to distinguish between certain modes and events (MAE). WaveExplorer allows for real time display and filtering. Posttest analysis features include threshold settings, filtering, event versus time plots, analysis based on energy of events, cross correlation, triangulation, and frequency content. Other features include the ability to determine the dispersion curves and velocity profile theoretically based on material properties for both isotropic and anisotropic materials.

Table 2. FM1 filtering and amplification capabilities.

	Gain (dB)	High Pass Filter (kHz)	Low Pass Filter (kHz)
Preamplifier	0-42 (in 6 dB Increments)	-	-
Acquisition Signal Conditioning	0, 12, 24	20, 50, 100	-
Trigger Signal Conditioning	0-42 (in 6 dB Increments)	50, 100, 300	750, 1500, 5000

5.2 Compact Portable Data Acquisition System (AIMS Box)

The automated impact monitoring system (AIMS) consists of a single box, sensors, and cabling. The AIMS box includes filters, preamplifiers, digitizers, and a power source in a single box for decreased size and portability (see Figure 37). The AIMS box does not have the capability of viewing the data for analysis. The AIMS box notifies engineers of an impact event through a text message sent from an internal cell phone. The data can be downloaded via file transfer protocol (FTP) over a LAN for analysis. The data can then by analyzed using Digital Wave's WaveExplorer or AIMS Beamforming software.

Figure 37. Automated Impact Monitoring System (AIMS) developed by Digital Wave Corporation in conjunction with ATK.

The AIMS box uses a single board computer limited to 16 MB of flash memory. Each wave file saved to the flash memory typically takes up less than 1 MB memory, allowing for multiple events to be recorded before the data must be deleted. The box is currently limited to 16 channels; however, it can be modified to the desired constraints of the system under investigation. The number to which the text message will be alerted can be modified and the text message tailored to any desired message.

Currently, the AIMS system operates at a sampling rate of 1 MHz but has the ability to sample at a rate up to 2 MHz. The filters are designed to filter out signals with frequencies less than 500 Hz and higher than 1 MHz and can be tailored to the particular structure under investigation. The settings for the amplifiers, sampling rates, and filters can also be adjusted for each particular structure under investigation, making it a very versatile tool for impact detection in the field.

5.3 Sensors

It is important to use a sensor that is optimized in performance to the particular material system being monitored. For accurate locating, it is imperative that the sensors be broadband damped sensors with a low Q value in order to distinguish between the plate wave modes. Traditional AE sensors are undamped highly resonant (high Q) narrow band sensors. The ringing induced in these sensors causes the wave modes to become indistinguishable, leading to highly inaccurate event locating. Figure 38 shows a comparison between an event detected using both a traditional and a MAE sensor.

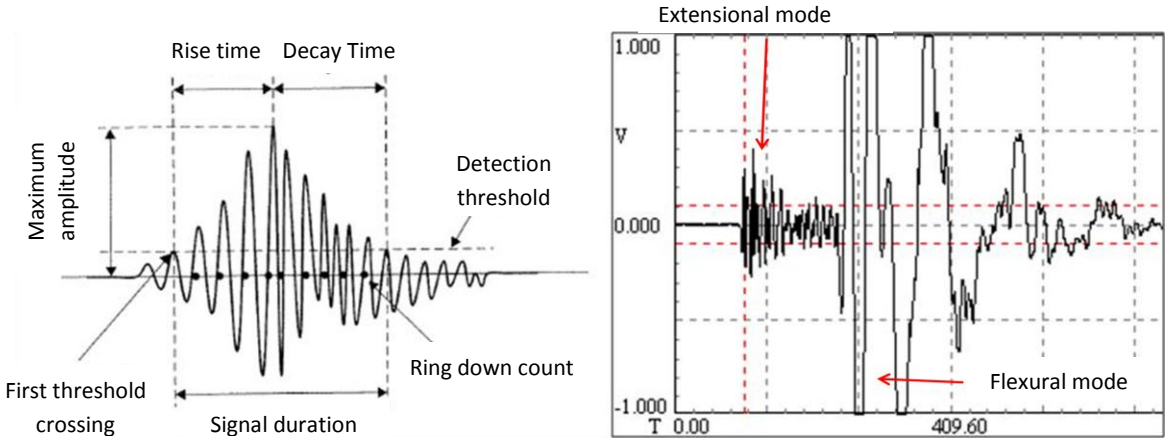

Figure 38. Difference in recorded waveforms between a) traditional and b) MAE sensors.

As such, various sensors were characterized to identify which sensor has the optimal response for use in an impact detection system. Currently, the lab system utilizes Digital Wave quarter inch diameter, B-225, and half inch diameter, B-225.5, sensors. These sensors are optimal for lab work; however, for a compact impact detection system, these sensors are too large with a height of one inch. Three other sensors, all film sensors, were characterized and evaluated against Digital Waves B-225 sensor. The following sections describe each sensor in some detail.

5.3.1 Digital Wave B-225 Sensor

Digital Waves B-225 and B-225.5 sensors are designed to operate at a frequency range of 1 kHz to 1.5 MHz. These sensors are made from piezoelectric elements operating with high fidelity. The operating temperature range is from -50^{0}C to 100^{0}C. The B-225 sensors are specifically designed to operate with high sensitivity in the lower

frequency range. The only difference between the B-225 and B-225.5 sensors is the diameter. The B-225.5 sensor is a half inch in diameter while the B-225 sensor is a quarter inch in diameter. The larger diameter sensor has the advantage of producing larger amplitude extensional modes (24). However, as discussed earlier, it is the flexural mode that should be utilized for increased accuracy at larger distances.

These sensors are especially useful in highly attenuative and thick plate materials, making them a very versatile sensor. For these reasons, the B-225 sensor will be the model to which all remaining sensors are compared (see Figure 39). These sensors are not to be used in the actual impact detection system due to the large size as well as the frequency bandwidth being just outside of the range desired (30 kHz to 300 kHz). For the two structures under investigation, it has been found that the typical impact propagates with a center frequency near 10 to 15 kHz. For these reasons, other sensors need to be utilized to increase the sensitivity at these lower frequencies as well as to decrease the size of the sensors footprint on the structure.

Figure 39. Digital Wave B-225 sensor.

5.3.2 Measurement Specialties SDT Film Sensor

The SDT film sensor is a piezoelectric film sensor made by Measurement Specialties[4]. The film element is rectangular in shape with a screen printed in silver ink folded over on itself providing a self-shielded transducer area good for working in areas with high EMI noise. The sensor can be applied to the material surface using double sided adhesives, epoxy, or super glue. The SDT film sensor can also be used as a contact microphone or a dynamic strain gage. This sensor has a frequency bandwidth of 1 Hz to 60 kHz and operates under temperatures ranging from 0^0C to 70^0C. The film element has a length of 1.18 inches, 0.51 inches in width, and a thickness of 0.005 inches, making it a good candidate for a low profile sensor with low cost (see Figure 40).

5.3.3 Measurement Specialties General Purpose FDT1-028K Film Sensor

The FDT sensor is similar to Measurement Specialties' SDT sensor except that it is not shielded and can be used as an ultrasonic transducer as well. As a contact ultrasonic transducer, the sensor has a low Q value. The piezoelectric element is also printed in silver ink but is not folded over on itself. The sensor can operate at a temperature range of -20^0C to 60^0C. The FDT sensor has a broad bandwidth operating from 1 Hz to 60 kHz making it also an ideal transducer for impact detection in the field. The sensor has dimensions similar to the SDT sensor (see Figure 41).

[4] Measurement Specialties, 1000 Lucas Way, Hampton, VA 23666, 1-800-745-8008

Figure 40. Measurement Specialties SDT film sensor.

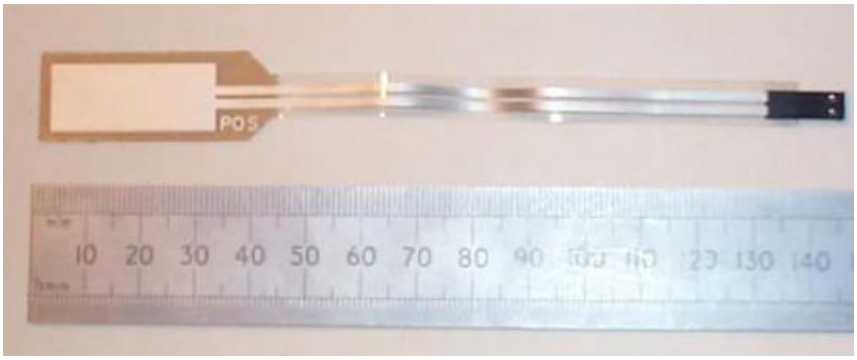

Figure 41. Measurement Specialties FDT film sensor.

5.3.4 Acellent's Single Smart Layer Ceramic Film Sensor

Acellent's[5] Smart Layer film sensors are high quality piezoelectric ceramic sensors. These sensors are placed on a polyamide high dielectric film that protects the sensor from the environment as well as EMI noise. The smart layer sensors can be used as an ultrasonic transducer as well as an MAE sensor. The ceramic element is a quarter inch in diameter and surrounded by a dielectric film with rectangular dimensions of 1.57 inches in length and 0.39 inches in width (see Figure 42). These sensors can also be

[5] Acellent Technologies, Inc. 835 Stewart Dr.Sunnyvale, CA 94085. 408-745-1188

Figure 42. Acellent's Smart Layer Ceramic film sensor.

made into strips including more than one sensor allowing for easier array setups. The smart layer sensors have a continuous operating temperature range of -55^{0}C to 120^{0}C and the ability to sense into the megahertz frequency range.

5.3.5 Sensor Comparison

Each film sensor was characterized in frequency and amplitude response and compared to Digital Wave's B-225 sensor. Tests were performed on the stiffness critical structure by placing each sensor side by side and pulsing a sine wave from a transmitting sensor at a given distance. Two B-225 sensors were used, one as the pulsar and one as a receiver to provide the baseline to which the remaining three film sensors are compared. The film sensors were each adhered to the structure by the use of Vishay M-Bond AE-10 adhesive while the B-225 sensors were coupled using Sperry multipurpose ultrasonic couplant. A function generator was used to drive the transmitting sensor while the recorded waveforms from each receiving sensor were stored and analyzed using the lab system. The transmitting sensor was moved further

away from the sensors for each test until a total distance of 84 inches from the receiving sensors to the transmitting sensor was achieved. This was done to determine if attenuation of the signal in a sandwich composite structure would alter the sensors response. The receiving sensors were amplified with a total gain of 80 dB in order to record the signal at all distances. Figure 43 shows the amplitude response as a function of frequency for each sensor as compared to the B-225 sensor.

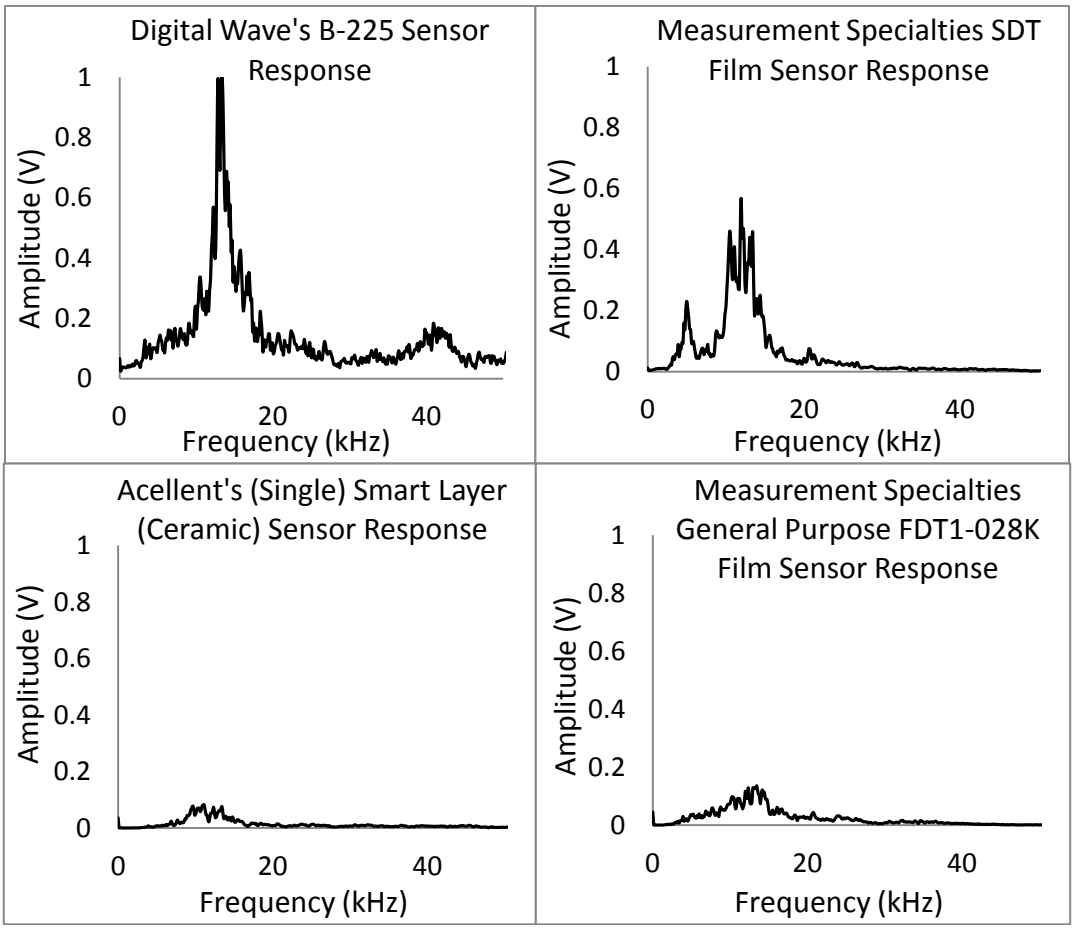

Figure 43. Frequency response of each sensor under investigation.

From Figure 43, it can be seen that the SDT film sensor developed by Measurement Specialties has the best response as compared to Digital Wave's B-225 sensor. The plots show the resulting enveloped response of the sensors as a function of frequency and distance. It was found that attenuation in the sandwich structure did not alter the frequency response of the sensors. It is suggested for field use that the SDT film sensors be used for impact detection.

5.4 Couplants

Couplant is also a very important part of the system since without it, transmission of the mechanical wave in the material system to the sensor would not be possible. Typically, a couplant with an acoustical impedance closest to that of the material system and the sensor is desired. For MAE, gel and grease couplants are normally used for lab testing while adhesives are used for field testing. Appendix B provides a more in depth look at what considerations should be kept in mind when determining the correct couplant to be used. The couplants chosen for use in this study are Sonotech's[6] High Z couplants for lab use and Vishay[7] M-Bond AE-10 adhesive for field use.

[6] Sonotech, Inc. 774 Marine Drive Bellingham, WA 98225. 360-671-9121
[7] Vishay. One Greenwich Place Shelton, CT 06484. 1-402-563-6866

CHAPTER 6

RESULTS

This section presents accuracy results from blind impacts performed on both the strength and stiffness critical structures using the beam steering algorithms developed in Chapter 4. The beam focusing algorithm is not included due to its inability to take into account anisotropic wave speeds and the dependence on distance between the impact and arrays, resulting in decreased confidence with increasing distance. Errors were determined experimentally on both the stiffness and strength critical structures to determine the true ability of the location algorithms to accurately locate events on full-scale complex components. The stiffness critical structure was used to filter out the various methods to determine the most robust algorithm for increased accuracy.

Two arrays using Digital Wave's B-225 sensors were used to detect the blind impact tests performed on both components. Each array consisted of four sensors connected to the lab system. Both arrays were placed parallel and in line with one another on opposite ends of the structure. For the stiffness critical structure, the arrays were spread apart vertically and for the strength critical structure, the arrays were spread along the length. Impacts were performed at various locations on the

component both far and near the arrays to cover a wide range of possible angles. The source of the blind impacts were then determined and compared to the actual source.

6.1 Stiffness Critical Structure

The same three methods used to determine the theoretical error plots for the stiffness critical structure in Chapter 4 are applied here to actual impacts performed on the structure. Random locations on the component were selected and actual impacts performed. The estimated sources of the actual impact locations were then calculated and error analysis performed. Using results found from both the theoretical and experimental errors, the methods with the greatest inaccuracy were removed for tests performed on the strength critical structure.

The results for each of the three methods are shown in Figure 44, Figure 45, and Figure 46. Table 3 shows the error analysis results found from the errors between the actual locations and the estimated locations using Equation 37. Note that the two arrays have the ability to cover over 65 ft^2 in area where each array is approximately 1 inch wide and 8 inches in length. As expected from the theoretical results, both the AIMS and velocity vector method show the best results. Unexpected, however, is that the average error using the velocity vector method shows the best results.

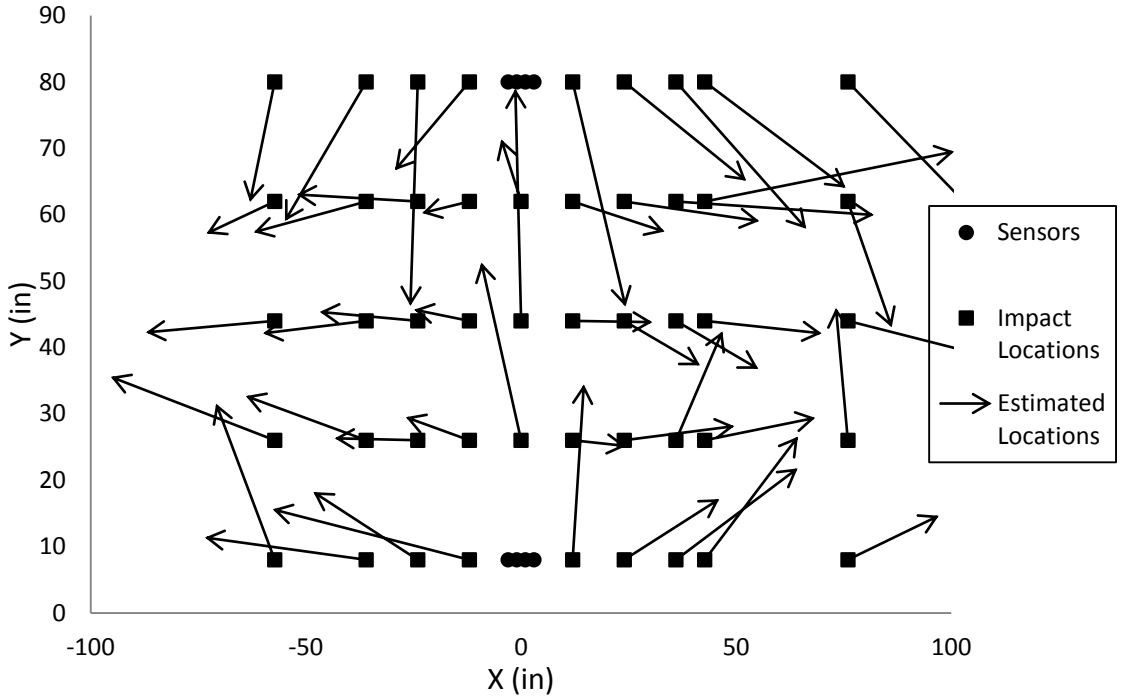

Figure 44. Results from experimental error analysis performed by blind impacts using the Quasi-Isotropic method on the stiffness critical structure.

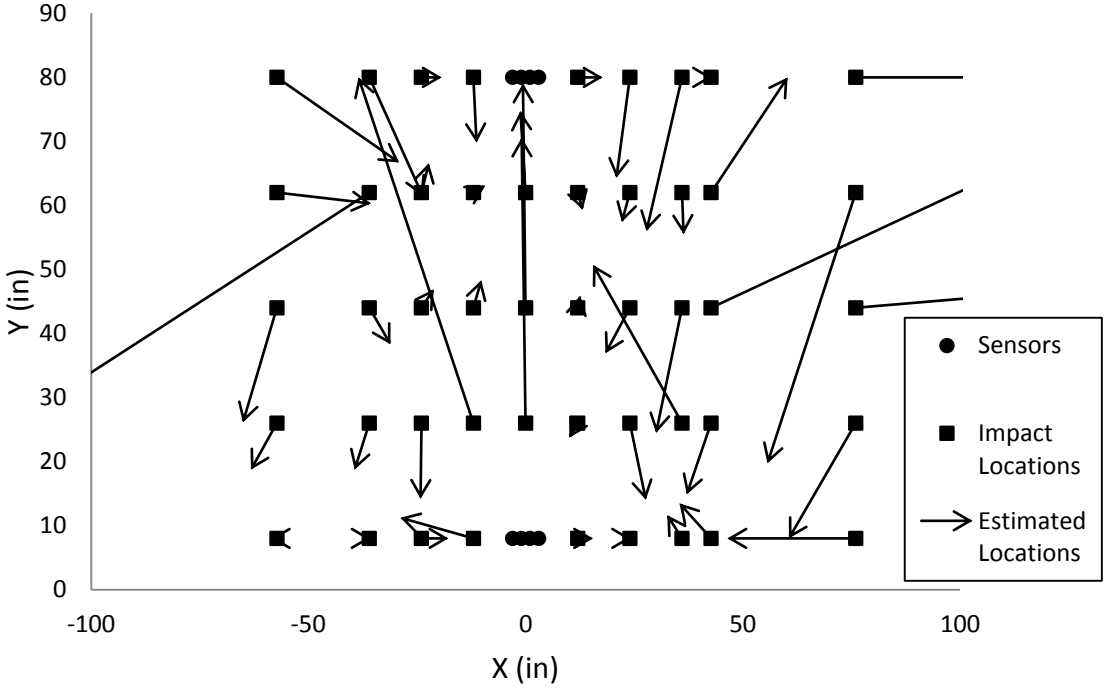

Figure 45. Results from experimental error analysis performed by blind impacts using the AIMS beam steering algorithm on the stiffness critical structure.

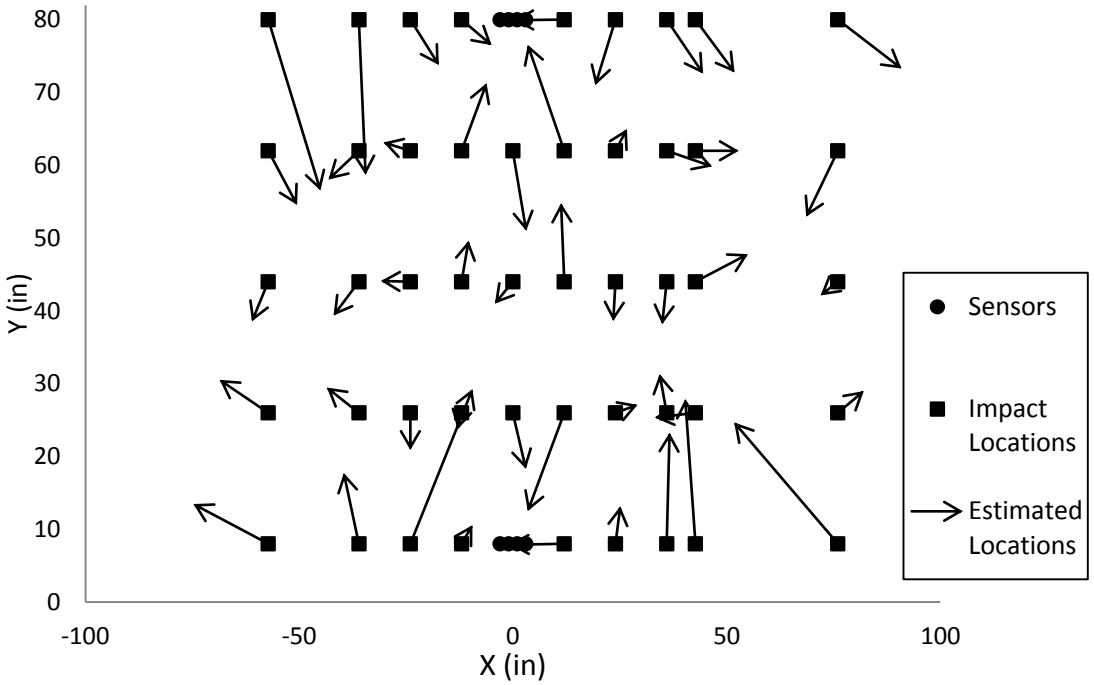

Figure 46. Results from experimental error analysis performed by blind impacts using the velocity vector approach on the stiffness critical structure.

Table 3. Error analysis results of the various location methods applied to actual impacts on the stiffness critical structure.

Covering over 65 ft²	Minimum (in)	Maximum (in)	Average (in)	Standard Deviation (in)
Quasi-Isotropic (QI)	3.90	116.69	63.60	28.13
AIMS	0.24	149.30	22.13	32.65
Velocity Vector	2.42	29.42	10.80	6.09

6.2 Strength Critical Structure

Impact location tests performed on the strength critical structure revealed some interesting results in the ability to precisely locate the source of events. The structure was implemented with two linear arrays placed parallel to one another on each end of the structure orientated such that the sensors lined up linearly around the circumference of the component. For these tests, Digital Wave's B-225 sensors were used along with the lab system.

The strength critical structure is designed with thickness changes on each end of the structure resulting in a region of tapering thickness and a liner on the inner surface of the cylinder. This phenomenon results in the wave speeds increasing or decreasing as the wave propagates over regions of changing thickness due to changes in stiffness and damping of the wave before propagating the full length of the structure due to the liner complicating the ability to accurately locate the source of events. As such, two arrays were placed in the midcylinder region of the structure where the thickness of the component is constant so as to initially neglect these variables in order to characterize the algorithms ability to locate. Figure 47 shows the blind impact locations relative to the arrays as well as the estimated locations using the velocity vector method. The area covered by the two 1 inch by 8 inch arrays is over 100 ft^2.

Table 4 shows the error analysis results from blind impacts performed on the strength critical structure using the velocity vector approach. Over a 100 ft^2 area the average error is approximately 9 inches, showing that for regions of constant thickness, the method can accurately locate events. It can be seen, however, that due to the

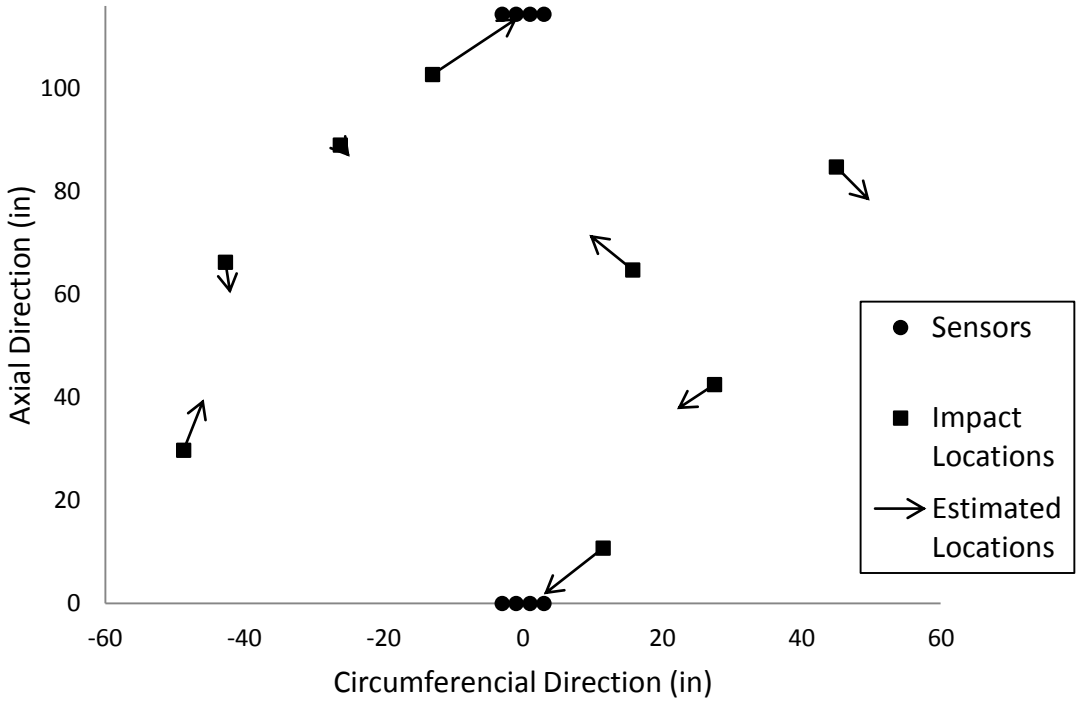

Figure 47. Estimated impact locations performed on the strength critical structure using the velocity vector method.

Table 4. Error analysis results from estimated impact data gathered on the strength critical structure using the velocity vector method.

Covering over 100 ft^2	Minimum (in)	Maximum (in)	Average (in)	Standard Deviation (in)
Velocity Vector Method	2.66	16.37	9.04	4.15

small diameter relative to the length, slight errors in the estimated angle from one array can result in large errors in the estimated location.

It was found that the vector velocity method works well on both strength critical and stiffness critical structures. However, if the material contains changes in thickness, the signal becomes distorted and causes changes in the wave speed of the propagating wave, resulting in very inaccurate estimated locations. Also, it was found that the addition of a liner on the inner surface of the strength critical structure damped out the flexural wave when traveling over large distances. Further work needs to be performed on complicated structures with changing thickness and the addition of materials that damp out the propagating wave to increase location capabilities.

CHAPTER 7

APPLICATIONS AND FUTURE WORK

As was shown, MAE coupled with phased array techniques provide the ability to increase accuracy of event location on anisotropic structures. However, MAE is not only useful for the detection and location of strength-reducing events. MAE can also aid in the detection and identification of elastic and inelastic events. When an impact occurs on the surface of a solid material, an elastic surface displacement occurs followed by the rapid release of energy due to fracture. MAE has the ability to distinguish between the elastic surface impact and fracture of the material. Figure 48 and Figure 49 show the resulting waveforms captured when an elastic and an inelastic impact are performed on an arbitrary material as well as the resulting load-versus-time plot. Notice that when an inelastic event occurs, the elastic surface impact event is followed by a much larger amplitude event due to the large release of energy due to fracture. Also notice that the load versus time indicates that at the point of damage formation, the stress drops as the material at the site of fracture strains.

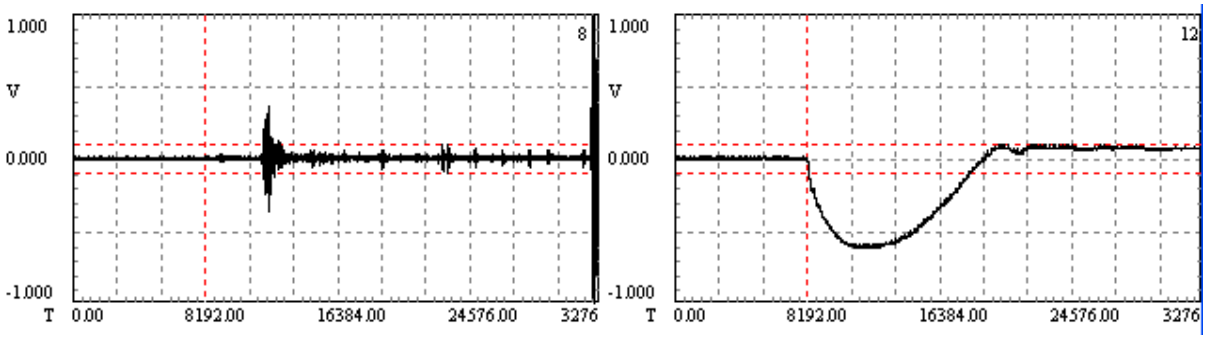

Figure 48. Elastic impact and the resulting MAE event on the left and the load versus time on the right.

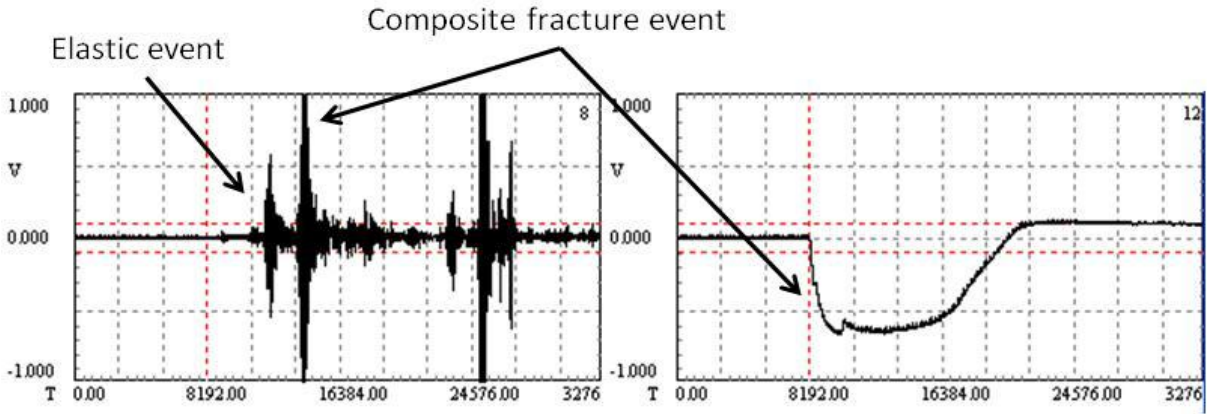

Figure 49. Inelastic event following the elastic surface impact and the recorded waveform on the left and the load versus time on the right.

Coupling the ability to detect fracture events with the location algorithms developed in this work, the ability to monitor a structure for strength-reducing events such as crack propagation and impact detection is possible. It should be noted that MAE cannot detect the nucleation/formation of damage in all cases; however, it has the ability to detect crack propagation and therefore can define an initiation point to characterize the rate of crack growth due to fatigue or other events. The MAE system can be attached to the structure permanently, providing a complete structural health

monitoring system capable of notifying the responsible engineer when a strength-reducing event has occurred for further inspection or repair. This type of system would be useful in applications such as aircraft and bridges due to its ability to monitor areas that cannot be inspected easily or cost effectively by traditional NDT methods.

MAE, when used as an active system, has the capability to detect various types of corrosive attach from pitting, reduction in thickness, and fluid parameters such as fluid level, composition, density, and obstruction in the pipeline (see references (25) and (26)). In 2003, Digital Wave designed and patented a system capable of detecting corrosion in pipes and containers using guided waves. Digital Wave found that by using the direct field method, detection of corrosive attack on above-ground pipelines is possible and the fluid parameters can be detected using the leaky field method. A reduction in thickness can be detected by both a reduction in the direct field and leakage fields.

As can be seen, MAE has a high potential for use as an integrated structural health monitoring system. Much work has been done and performed to expand the use and knowledge of its applications; however, its uses and applications are still not fully matured. Further work should be focused on developing methods to more accurately locate in regions of varying thickness as well as long, slender thin-walled cylindrical structures. Future work should focus on relating the physics behind the relationship between the beam steering time delay laws and the vector velocity method to increase location accuracy as well as the deconvolution of MAE waveforms to directly identify the modes of damage occurring when inelastic events are detected. The ability to

deconvolve the wave to determine the type of damage mode occurring can greatly reduce inspection time by providing the ability to determine if the damage mode occurring was larger than the design allowable damage size. This would mean use of more traditional methods such as ultrasound would not be necessary to interrogate the material to determine the extent of damage and that this system would be able to monitor the structure in real time. As such, more work should also be performed on developing a smaller more compact portable data acquisition system to reduce size and weight of the system.

CHAPTER 8

CONCLUSION

In an attempt to decrease manufacturing costs of composite structures, designers are attempting to design to Barely Detectable Damage (BDD). Decreasing the critical damage size to BDD implies that steps must be taken to reduce the risk of damage induced after the component leaves the manufacturing facility and while in service. Using passive modal acoustic emissions (MAE), a low profile, low sensor density impact detection system was developed to mitigate these issues that is capable of detecting impacts and other strength-reducing events and accurately locate the source.

Tests were performed on both strength and stiffness critical structures. The system developed coupled concepts from phased array beam steering techniques and MAE to reduce the number of sensors and cabling while increasing the accuracy of event locating on anisotropic materials. Various types of film sensors were characterized for both attenuation and frequency response in order to optimize the detection capabilities and reduce the sensor footprint. Measurement Specialties' SDT film sensor was chosen as its response was the most comparable to Digital Wave Corporation's B-225 ceramic sensors used in the lab. In conjunction with Digital Wave

and ATK, a compact portable data acquisition system (AIMS box) was manufactured. When impacts occur, the AIMS box notifies the responsible engineer through a text message sent from an internal cell phone. The data can then be downloaded and location analysis performed.

Impact location results show that the detection system is capable of locating impacts on strength and stiffness critical structures with high accuracy. Both structures utilized two 1 inch by 8 inch arrays consisting of four sensors each. Results from the stiffness critical structure show that over a 65 ft^2 area, the average error in the estimated source location is approximately 11.0 inches. For the strength critical structure, impact location was performed over a 100 ft^2 region with an average error of 9.0 inches. However, full coverage of the strength critical structure found errors to be high due to the small diameter-to-length ratio, changes in thickness, and the addition of materials that dampen out the propagating wave. Changes in thickness were found to cause the wave speed of the plate waves to change due to changes in stiffness affecting the ability to locate the source with high precision. The addition of damping materials caused the waves to attenuate before the wave reached the full length of the structure to the receiving sensors. It was found that structures with a small diameter to length can cause large errors due to small inaccuracies of the estimated angle from the sensor arrays to the source. For structures with small diameters to length ratio's, regions of changing thickness, and the addition of damping materials, more work needs to be performed to increase the ability to locate with high precision.

As was demonstrated in this work, use of a passive MAE system coupled with phased array techniques can be beneficial as a SHM system. The system has the ability to detect strength reducing events and accurately locate the source for decreased inspection times and time out of service. MAE also can provide the ability to detect crack propagation and therefore can be used to characterize crack propagation rates due to fatigue or other events of structure while in service.

APPENDIX A

LAMINATE PLY ORIENTATION CODE

The following shows how to apply the laminate ply orientation code for a composite structure. The axial direction (x-axis) is typically taken as the 0^0 orientation, the transverse in-plane direction as the y-axis, and the thickness direction perpendicular to the xy plane as the z-axis. A laminate is composed of several layers of lamina. The following few rules can be used to decipher the laminate ply orientation code:

- Each ply is designated by its fiber orientation angle in the global coordinates
- Ply's are listed in sequence beginning from the top surface of the laminate
- Ply's are separated by a "/" if their angles are different
- If adjacent ply's are positioned at the same angles, a subscript can be used (ex. 30_2)
- Brackets denote a complete laminate
- Over bars mean do not repeat ply in sequence
- Subscript "S" denotes a midplane symmetry

- Subscript “T” denotes total laminate symmetry
- $\mp$ mean negative first then positive and $\pm$ visa versa

The following shows how the rules can be used to write the ply orientations for the laminates shown in Figure 50:

a) $[(90/0/\mp 45)_2]_T$ or as $[90/0/\mp 45]_{2T}$

b) $[(0/45)_2/\overline{90}]_S$

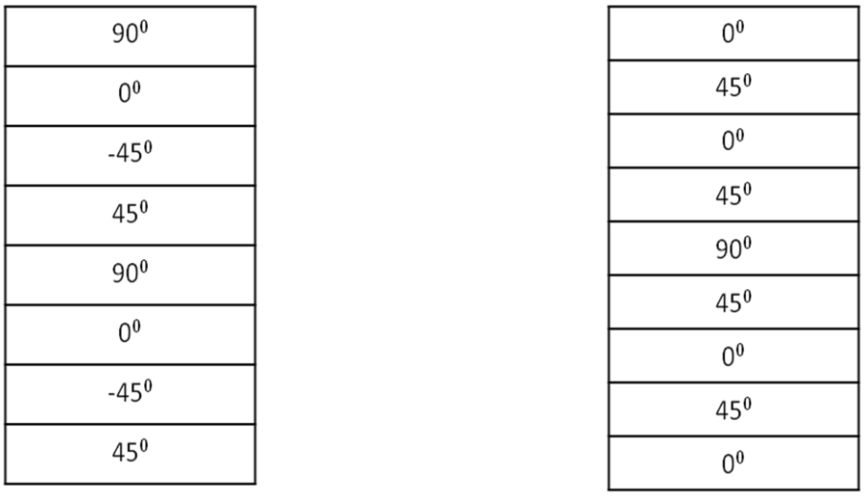

Figure 50. Two laminate ply orientations for use in applying the laminate orientation code.

APPENDIX B

COUPLANTS

In order for a sensor to convert a mechanical wave into an electrical signal properly, it must be properly coupled to the medium supporting the wave. If the sensor is not coupled properly, some of the waveform amplitude or frequency content, if not all, maybe lost (27). Different couplants will transfer the mechanical wave differently and therefore, care must be taken when choosing the correct couplant. Various considerations must be taken into account when choosing the couplant to be used. Some of the things to consider when choosing a couplant are:

- Period in which the sensor must be coupled to the structure
- Frequency in which the sensor will be removed from the structure
- Whether or not the sensor can be permanently attached to the structure
- Will the environment/surroundings induce any movement or vibrations that can disrupt the sensor position
- Conditions of the surrounding environment (temperature, humidity)
- Will the couplant react with the material in which its being applied to (such as corrosion)

One of the most important characteristics for optimizing the couplant's transmission ability is the couplant's acoustical impedance. The couplant's primary focus is to remove any air between the material and the sensor. The impedance of air is much lower than the impedance of the material and the sensors face, causing a large impedance mismatch. This impedance mismatch causes a large loss in transmission of the waveform from the material to the sensor. Introducing a couplant that has an impedance closer to that of the material and sensor face will displace the air and increase the signal transmission to the sensor. An alternative to the use of couplants is to apply large amounts of force to the sensor to displace any air between the sensor face and the material. This method, however, will still induce a lower transmission coefficient than that for using couplants and is not advisable.

Many different types of couplants exist, typically in the form of liquid, gel, adhesives, or grease. Since it is the flexural mode of interest, largest particle motion normal to the plane of the plate, the viscosity of the couplant is not of great importance. If the extensional mode was of interest, the viscosity of the couplant would be an important factor for transmission of the shear wave to the sensor (28). The following describes some of the characteristics of basic types of couplants.

Liquid Couplants

Liquids work well on smooth surfaces and are easily applied; however, as a down-side, liquids have a lower acoustical impedance. With a lower viscosity, liquids should not be used on surfaces where the sensor is to be mounted vertically or upside

down as they tend to run and dry up quicker then gels and grease couplants. Also due to the lower viscosity, transmission of the extensional mode will not be optimized. Liquids should not be used on tests requiring more than a few hours of testing due to the quick drying time. With a low viscosity, the sensors will need mounting fixtures to hold the sensors in place over the couplant. Liquid couplants, due to their ease in application, are also easily removed, making them ideal for use in the lab.

Gel Couplants

Gel couplants are also easy to apply and clean up but have a higher viscosity than liquid couplants, making them more ideal for vertical and upside-down applications. Gels typically have higher acoustical impedance than liquid couplants and, due to their higher viscosities, are better for rougher surfaces. Gels will also dry out quick with time, especially near the edges of the transducer, and should only be used for short period tests. Corrosion inhibitors can also be included in the gel to help minimize any chemical reactions between the sensor and material system under investigation.

Adhesive Couplants

Adhesives do not require any clamping mechanisms to hold the sensor to the material system but instead bond the sensor to the material. This type of couplant is good for permanently attaching the sensors to a structure and when complete stability of the sensor on the surface of the structure is required. In field use, the structure may be subjected to vibrations which can loosen the sensor's bond to the structure and

compromise the transmission of the wave from the material to the sensor. For such reasons, it is suggested that some type of adhesive such as a rubber compound or cyanoacrylate adhesive be used when long term-testing is required. Adhesive couplants will transmit the extensional wave as well as high viscosity gels and grease couplants. When choosing the type of adhesive to be used, it is important to check the manufactures specifications for long-term stability. After the adhesive has been fully cured, the bond with time may change, particularly the shear modulus, altering the acoustical performance of the couplant. Once the sensor has been applied with an adhesive, removal will likely damage the sensor; therefore, adhesives should only be used for testing in the field.

REFERENCES

1. Department of Defense. *Composite Materials Handbook: Volume 3*, 2002.

2. Morgan, M.E.; Madsen, C.B.; Watson, J.O. *Damage Screening Methodology for Design of Composite Rocket Motor* Cases, JANNAF Propulsion Meeting, Indianapolis, 1992.

3. Zhou, Xu. ATK Aerospace Structures, Senior Design and Analysis Engineer, Clearfield, UT. Personal Communication, March 2010.

4. Tobias, A. Acoustic-Emission Source Location in Two Dimensions by an Array of Three Sensors. *J. NDT* **1976**, 9, 9-12.

5. Viktorov, I.A. *Rayleigh and Lamb Waves: Physical Theory and Applications*; Plenum Press: New York, 1967.

6. Gorman, M.R. Plate Wave Acoustic Emission. *J. Acoust. Soc. Am.* **1991**, 358-368.

7. Gorman, M.R.; Prosser, W.A. AE Source Orientation by Plate Wave Analysis. *J. Acoust. Emissions* **1991**, 9, 283-288.

8. Rogers, W.P Elastic Property Measurement Using Rayleigh-Lamb Waves. *J. of RNDE* **1995**, 6, 185-208.

9. Andreikiv, O.E.; Skal's'kyi, V.R.; Serhienko, O.M. Acoustic Emission Criteria for Rapid Analysis of Internal Defects in Composite Materials. *J. Mater. Sci.* **2001**, 37, 106-117.

10. Guo, S.S.; Cawley, P. The Interaction of Lamb Waves with Delaminations in Composite Laminates. *J. Acoust. Soc. Am.* **94**, 2240-2246.

11. Kessler, S.S.; Spearing, M.S.; Soutis, C. Damage Detection in Composite Materials using Lamb Wave Methods. *J. Smart Mater. Struct.* **2002**, 11, 269-279.

12. Diamanti, K.; Hodgkinson, J.M.; Soutis, C. Detection of Low Velocity Impact Damage in Composite Plates using Lamb Waves. *J. SHM* **2004**, 3, 33-41.

13. Toyama, N.; Takatsubo, J. Lamb Wave Methods for Quick Inspection of Impact-Induced Delamination in Composite Laminates. *J. Composite Sci. Tech.* **2004**, 64, 1293-1300.

14. Diamanti, K.; Soutis, C.; Hodgkinson, J.M. Lamb Wave for the Non-Destructive Inspection of Monolithic and Sandwich Composite Beams. *J. of Composites Part A: Applied Sci. and Manufacturing* **2005**, 36, 189-195.

15. Diamanti, K.; Soutis, C.; Hodgkinson, J.M. Piezoelectric Transducer Arrangement for the Inspection of Large Composite Structures. *J. of Composites Part A: Applied Sci. and Manufacturing* **2007**, 38, 1121-1130.

16. Vishnuvardhan, J.; Muralidharan, A.; Krishnamurthy, C.V.; Balasubramaniam, K. Structural Health Monitoring of Anisotropic Plates using Ultrasonic Guided Wave STMR Array Patches. *J. NDT&E Int.* **2009**, 42, 193-198.

17. Ramm, O.T.V.; Smith, S.W. Beam Steering with Linear Arrays. *J. of IEEE Trans. on Biomed. Engin.* **1983**, 30, 438-452.

18. Wooh, S.C.; Shi, Y. Optimum Beam Steering of Linear Phased Arrays. *J. of Wave Motion* **1999**, 29, 245-265.

19. Talreja, R. Damage Development in Composites: Mechanisms and Modeling. *J. of Strain Analysis* **1989**, 24, 215-222.

20. Deemer, C.M. Use of Plate Waves for Predicting Remaining Useful Life of Ceramic Matrix Composites. Ph.D. Dissertation, Northwestern University, Evanston, IL, 2003.

21. Hutchins, D.A.; Lundgren, K. A Laser Study of Transient Lamb Waves in Thin Materials. *J. of Acoustical Soc. Am.* **1989**, 85, 1441-1448.

22. Tipler, P.A.; Llewellyn, R.A. *Modern Physics*, 4th ed.; 2003; pp 215-221.

23. Christensen, D.A. *Ultrasonic Bioinstrumentation*; 1998.

24. Huang, W. *Application of Mindlin Plate Theory to Analysis of Acoustic Emission Waveforms in Finite Plates*; Report; Digital Wave Corporation, Englewood, CO, 1998.

25. Gorman, M.R.; Ziola, S.M. Noninvasive Detection of Corrosion, MIC, and Foreign Objects in Containers, using Guided Ultrasound Waves. U.S Patent 6,363,788 B1, April 2, 2002.

26. Gorman, M.R.; Ziola, S.M.; Huang, W. Noninvasive Detection of Corrosion, MIC, and Foreign Objects in Fluid-Filled Pipes using Leaky Guided Ultrasonic Waves. U.S. Patent 6,595,059 B2, July 22, 2003.

27. Colombo, S.; Giannopoulos, A.; Forde, M.; Hasson, R.; Mulholland, J. Frequency Response of Different Couplant Materials for Mounting Transducers. *J. of NDT&E Int.* **2005**, 38, 187-193.

28. Dugmore, K.; Jonson, D.; Walker, M. A Comparison of Signal Consistency of Common Ultrasonic Couplants Used in the Inspection of Composite Structures. *J. of Composite Struct.* **2002**, 58, 601-603.